

Comparing the performance of practical two-qubit gates for individual ^{171}Yb ions in yttrium orthovanadate

Mahsa Karimi,^{1,*} Faezeh Kimiaee Asadi,¹ Stephen C. Wein,^{1,†} and Christoph Simon¹

¹*Institute for Quantum Science and Technology, and Department of Physics & Astronomy, University of Calgary, 2500 University Drive NW, Calgary, Alberta T2N 1N4, Canada*

In this paper, we investigate three schemes for implementing Controlled-Z (CZ) gates between individual yttrium (Yb) rare-earth ions doped into yttrium orthovanadate (YVO₄ or YVO). Specifically, we investigate the CZ gates based on magnetic dipolar interactions between Yb ions, photon scattering off a cavity, and a photon interference-based protocol, with and without an optical cavity. We introduce a theoretical framework for precise computations of state and gate infidelities, accounting for noise effects. We then compute the state fidelity for each scheme to evaluate the feasibility of their experimental implementation. Based on these results, we compare the performance of the two-qubit gate schemes and discuss their respective advantages and disadvantages. We conclude that the probabilistic photon interference-based scheme offers the best fidelity scaling with cooperativity and is superior with the current technology of Yb values, while photon scattering is nearly deterministic but slower with less favourable fidelity scaling as a function of cooperativity. The cavityless magnetic dipolar scheme provides a fast, deterministic gate with decent fidelities if close ion localization can be realized. While focusing on $^{171}\text{Yb}^{3+}$: YVO system as a case study, the theoretical tools and approaches developed in this work are broadly applicable to other spin qubit systems.

I. INTRODUCTION

Two-qubit gates are fundamental for enabling entanglement swapping in quantum repeaters [1, 2] and are crucial for generating and mapping entangled states in distributed quantum computing [3]. From a computational standpoint, these gates are essential for universal quantum computation, as they enable the efficient decomposition of arbitrary quantum gates into circuits composed of Controlled-Z (CZ) and single-qubit gates [4, 5].

For the practical implementation of quantum computing, various experimental platforms have been explored, including solid-state systems such as superconducting qubits [6], quantum dots [7], and impurity-doped solids like rare-earth ions (REIs) embedded in crystals [8] and nitrogen-vacancy (NV) centers in diamonds [9]. Among these solid-state systems, REIs doped into crystals are known because of their remarkable coherence properties [10, 11]. The relatively low radiative decay rate of REIs [12] can be significantly improved by coupling them to a nanophotonic optical cavity, which enhances their emission through Purcell enhancement [13, 14]. Additionally, incorporating a cavity boosts photon collection efficiency and improves single-photon indistinguishability.

Within rare-earth ions (REIs), Kramers ions, which have an unpaired electron in their f shell such as erbium (Er^{3+}), neodymium (Nd^{3+}), and ytterbium (Yb^{3+}) exhibit substantial magnetic moments on the order of the Bohr magneton (μ_B). Thus, these ions can interact with nearby ions through magnetic dipole-dipole interactions. Among Kramers REIs, Yb^{3+} is known for its simple level structure, comprising of two electronic multiplets for the ground ($^2F_{7/2}$) and excited ($^2F_{5/2}$) states. Notably, $^{171}\text{Yb}^{3+}$ isotope of Yb^{3+} is the only Kramers rare-earth ion with the lowest nuclear spin of $I = 1/2$. Hence,

it benefits from long coherence times of nuclear levels [15], while maintaining the simplest possible hyperfine energy level structure with only a few narrow transitions in the optical absorption spectra [16, 17]. This simplicity facilitates more efficient manipulation of spin qubits and gate operations. Consequently, Yb is an attractive candidate for practical applications in rare-earth quantum information processing [18–28].

Among host crystals, Yb ions doped into yttrium orthosilicate (Y_2SiO_5 or YSO) and yttrium orthovanadate (YVO₄ or YVO) have been extensively studied [16–18]. YSO is widely used in quantum experiments, primarily due to the small magnetic moments of its components [29]. Conversely, YVO is of interest due to its high site symmetry, leading to narrow inhomogeneous linewidths when doped with $^{171}\text{Yb}^{3+}$ [17]. YVO is also promising for fabricating nanophotonic cavities [30], and particularly for Yb: YVO [31, 32], making it a compelling choice for this study.

Thus far, the design of quantum gates with large ensembles of REIs has been studied [33–35]. However, scalability issues with these designs [36] have prompted a shift toward using individual ions [37–40]. In that regard, significant advancements have been made in addressing individual rare-earth ions, particularly with praseodymium [41], erbium [42, 43], ytterbium [31], and neodymium ions coupled to a photonic crystal resonator [44]. Recent experimental progress has achieved probabilistic generation of maximally entangled state between individual $^{171}\text{Yb}^{3+}$ ions located in remote cavities [45]. Despite these advances, there has yet to be an experimental implementation of CZ gates between single REIs.

To implement two-qubit gates between individual rare-earth ions, various interaction mechanisms have been proposed. These include electric [46, 47], magnetic dipolar [8, 48], and cavity-mediated [49] interactions.

In [48], the authors have compared Controlled-NOT (CNOT) gates based on phase-accumulation and blockade mechanisms utilizing magnetic dipole-dipole interaction. They have shown that leveraging the full interaction strength, the magnetic dipolar phase-based scheme is faster and less

* mahsa.karimi1@ucalgary.ca

† Current affiliation is Quandela, 7 Léonard De Vinci, 91300 Massy, France.

constrained by the distance between ions compared to the magnetic dipolar blockade gate scheme. In contrast to dipolar gates, cavity-mediated interaction gates do not require qubits to be in close proximity. Instead, these gates rely on the presence of a cavity, which may also be necessary for other purposes, such as improving interfaces between stationary qubits (like quantum emitters) and flying qubits (like photons). Therefore, it is important to explore and compare the advantages of cavity-based and cavityless two-qubit gates between individual Yb ions, evaluating their implementation feasibility more thoroughly.

In this paper, we compare two-qubit gates between individual $^{171}\text{Yb}^{3+}$ ions, focusing on schemes that hold practical promise in the near to medium term, given the current state of the technology. Specifically, we explore the phase accumulation gate based on magnetic dipolar interactions, cavity-mediated photon scattering, as well as a photon interference-based scheme, both with and without an optical cavity.

A key figure of merit for assessing the performance of a gate scheme is the fidelity (F). Notably, $1/(1-F)$ provides an estimate of the number of gate operations that can be performed without the need for quantum error correction [48, 50]. Consequently, high-fidelity gates are essential for fault-tolerant quantum computing and first-generation quantum repeaters. To understand the sensitivity of each gate scheme to error parameters, we develop a theoretical framework to compute fidelity. We model the evolution of our system using the Gorini–Kossakowski–Sudarshan–Lindblad (GKSL) equations [51]. By computing perturbed solutions to the corresponding GKSL equations, we derive closed-form expressions for calculating infidelities. Our perturbative approach captures noise-induced errors through a formulation that relies merely on the noise parameters and the solution of the noiseless system, thus avoiding the need to solve the GKLS master equation directly. Therefore, our results offer a more feasible computational method compared to existing literature [49, 52, 53]. Concretely, denoting the system size by d , our method’s computational cost scales as $O(d^3)$ as opposed to $O(d^6)$ being the cost of computation in prior works. Furthermore, as highlighted by [54], the connection between the Lindbladian and error rates is still being uncovered, and our work can be considered one step further in that direction. These results can be applied to estimate single- and two-qubit gate errors of a given system, laying the foundation for universal quantum computing.

Using the above-mentioned perturbative approach we report the state and gate fidelities of the magnetic dipolar gate scheme presented in this work. We then discuss the requirements for implementing these gates within the Yb:YVO system, comparing the performance of each scheme based on current experimental technology. We also highlight their respective advantages and disadvantages, providing a comparative framework to guide the selection of the most suitable approach.

We note that while this comparison study focuses on the $^{171}\text{Yb}^{3+}$:YVO system, the mathematical tools and methodologies presented in this work can be applied to other

spin qubits, including other rare-earth ions in various host materials and defect centers in materials such as diamond, silicon, or silicon carbide.

The paper is structured as follows: In [Section II](#), we introduce the Yb ion system. [Section III](#) investigates the two-qubit gate schemes. The details of the perturbative approach for computing the fidelities are presented in [Section IV](#). In [Section V](#), we analyze the fidelity calculations for the gate schemes. We also discuss the practical implementation of key parameters influencing the fidelities, along with the current achievable fidelity for Yb ions. In [Section VI](#), we compare the different gate schemes and provide the pros and cons of each. Finally, we conclude and present an outlook in [Section VII](#).

II. YB RARE-EARTH ION PROPERTIES

$^{171}\text{Yb}^{3+}$:YVO has four Kramers doublets in the ground state and three in the excited state. At low temperatures, only the lowest doublet is populated. [Figure 1](#) illustrates the energy level structure of this system in the presence of a magnetic field [17, 55]. Within a Kramers doublet, the effective spin Hamiltonian of the Kramers ions with non-zero nuclear spin, I , can be written as [56]

$$H_{\text{eff}} = \mu_B \mathbf{B} \cdot \mathbf{g} \cdot \mathbf{S} - \mu_N \mathbf{B} \cdot \mathbf{g}_N \cdot \mathbf{I} + \mathbf{A} \cdot \mathbf{S} \cdot \mathbf{I} + \mathbf{I} \cdot \mathbf{Q} \cdot \mathbf{I}, \quad (1)$$

where μ_B (μ_N) is the electronic (nuclear) Bohr magneton, \mathbf{B} is the external magnetic field, \mathbf{S} (\mathbf{I}) is the electronic (nuclear) spin operator, \mathbf{g} (\mathbf{g}_N) is the electronic (nuclear) Zeeman tensor, \mathbf{A} is the hyperfine tensor, and \mathbf{Q} is the electronic-quadrupole tensor. For ^{171}Yb , $\mathbf{I} \cdot \mathbf{Q} \cdot \mathbf{I} = 0$, because this term only appears for ions with $I \geq 1$ facilitating the spectroscopic properties analysis of this isotope comparing to $^{167}\text{Er}^{3+}$ with $I = 7/2$ [16].

III. GATE SCHEME DESCRIPTIONS

In this section, we discuss practical two-qubit gate schemes involving individual $^{171}\text{Yb}^{3+}$ ions doped into YVO crystals (see [Table I](#)). With a focus on near- to medium-term feasibility based on the current state of technology, we outline the rationale behind our scheme selection.

Among deterministic two-qubit gates, those based on the dipolar interactions have the advantage of not requiring a cavity for their implementation. However, for Yb:YVO, there is no information on the change in the permanent electric dipole moment ($\Delta\mu$) mainly due to the lack of a first-order DC Stark shift, a limitation arising from the site symmetry [31]. This inherent characteristic significantly hinders the implementation of electric dipolar gates, including both blockade-based and phase-accumulation schemes, in the Yb:YVO system. Nevertheless, magnetic dipolar interaction-based gates, such as blockade and phase-accumulation schemes, remain viable for this system. However, as shown in [48], a comparison of

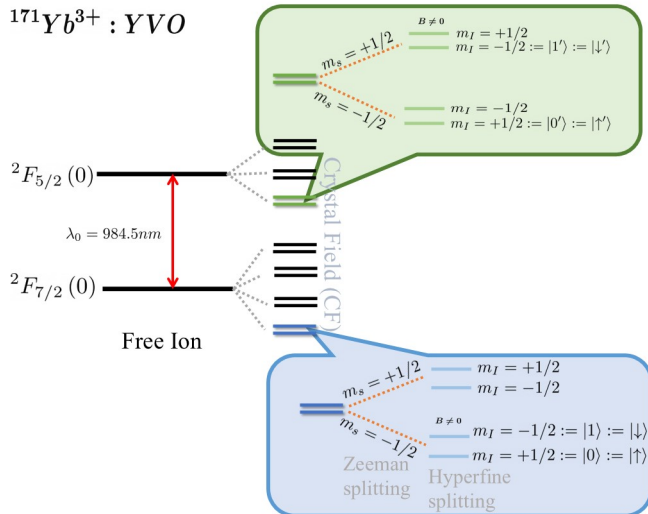


FIG. 1. The level structure scheme of $^{171}\text{Yb}^{3+}$ ions doped into YVO crystal, where a high magnetic field separates the electron and nuclear spin mixing.

these two approaches reveals that the magnetic blockade gate, which relies on frequency shifts, is a promising scheme for ions' separation in the order of 1 nm. Given the challenge of identifying such closely spaced Yb ion pairs, we focus on the magnetic phase-accumulation scheme, which provides relatively greater flexibility in terms of separation distance between the ions and operates significantly faster than the magnetic blockade gate [48].

Among cavity-mediated two-qubit gates, as demonstrated in [49], the photon scattering achieves higher fidelity with lower cavity cooperativity requirements. This is particularly relevant for the Yb: YVO system (and more generally for REIs), where achieving high cooperativity is challenging. Although the photon scattering gate scheme is intrinsically deterministic, a non-ideal photon detection process may result in a gate efficiency of less than one [57]. Additionally, the photon interference-based scheme currently being explored experimentally for Yb:YVO system [45] shows promising results for entanglement generation. However, this scheme is constrained by a success probability of only 50%.

Therefore, in the first approach, following [48], we focus on the magnetic dipolar interaction of Yb ions to implement a two-qubit gate between two ground states by inducing a phase difference between two excited states within the ions. In our second approach, following [49], we discuss a cavity-mediated interaction, including scattering a single photon off a cavity-ion system to execute a CZ gate between two Yb ions. In the third approach, based on [58], we explore a photon interference-based entanglement generation protocol that can be adapted into a CNOT gate between Yb ions. We demonstrate that incorporating a cavity can enhance the fidelity of this gate.

A. Magnetic dipolar interaction gate scheme

As suggested in [8, 48], one can exploit the magnetic dipolar interaction between two Yb ions to perform a two-qubit phase gate. In our setup, we consider two nearby Yb ions doped into YVO. For each ion, we define a “passive qubit” by utilizing two of the lowest hyperfine ground state energy levels that share the same electron spin but differ in nuclear spins. We denote these levels as $|\uparrow\rangle$ and $|\downarrow\rangle$, as depicted in Figure 2. These passive qubits have a long coherence time (31 ms [31]) and therefore can serve as memory qubits. However, for the gate operation, to speed up the slow microwave couplings, mitigate microwave-induced interactions on nearby ions and enhance the interaction strength, the quantum state of passive qubits must be transferred to “active qubits” in the excited state, which possess a significantly different g-tensor compared to the ground state [8, 48]. For each Yb, we define active qubit levels using a different electronic spin level. This selection allows the active qubits to interact via the electronic magnetic dipolar interaction, which is proportional to μ_B , rather than the nuclear magnetic dipolar interaction, which is proportional to μ_N [48]. Here, we define the active qubit levels using solid green lines and denote them by $|\uparrow'\rangle$ and $|\downarrow'\rangle$ as shown in Figure 2. We describe this selection in Section V A. In the following, we examine the magnetic dipolar interactions between active qubits to design a two-qubit gate between two Yb ions.

First, each Yb ion should be initialized in the lowest hyperfine ground state ($|\uparrow\rangle$) through optical pumping. Next, applying a $\pi/2$ microwave pulse can create a superposition of the $|\uparrow\rangle$ and $|\downarrow\rangle$ states. Following this, the population is transferred from the passive qubits to the active qubits by applying four π pulses (P_1) simultaneously (two on each ion) as shown in Figure 2. This results in the transitions $|\uparrow\rangle \mapsto |\uparrow'\rangle$ and $|\downarrow\rangle \mapsto |\downarrow'\rangle$, placing each Yb ion into a superposition of $|\uparrow'\rangle$ and $|\downarrow'\rangle$. At this stage, the magnetic dipole-dipole interaction between the active qubits performs a two-qubit phase gate. Specifically, if the control qubit (the first qubit) is in state $|\uparrow'\rangle$, the phase of the target qubit (the second qubit) remains unchanged. Conversely, if the control qubit is in state $|\downarrow'\rangle$, it induces a phase change in the target qubit. Finally, after a time delay, the quantum states are brought back to the passive qubits by applying another set of π pulses (P_2). A schematic representation of this process is shown in Figure 2.

Note that to perform a CZ gate between passive qubits, additional single-qubit gates are required in conjunction with the above phase gate

$$\text{CZ}^{(1)} = (\sqrt{Z} \otimes \sqrt{Z})U_1 \quad (2)$$

where \sqrt{Z} for a Pauli Z is defined as $\sqrt{Z} := \exp(-i\frac{\pi}{4}Z)$, and $U_1 = \exp(i\frac{\pi}{4}(Z \otimes Z))$ is the unitary implemented by the Ising interaction. Once we have a CZ gate, a CNOT gate also can be achieved by applying two Hadamard gates on the target qubit $\text{CNOT} = (\mathbb{I} \otimes H)\text{CZ}(\mathbb{I} \otimes H)$. Single qubit gates can be performed on passive qubits either through microwave fields or with the help of active qubits through optical fields [48].

Gate Schemes	Determinism	Medium	Dominant error	Infidelity scaling	# Levels
Magnetic dipolar	deterministic	crystal bulk	ions' separation	$O(r^3)$	4
Photon scattering	near deterministic	cavity	cooperativity	$O(C^{-\frac{2}{3}})$	3
Photon interference-based	probabilistic	bulk or cavity	cooperativity	$O(C^{-1})$	3

TABLE I. Two-qubit gate schemes discussed in this paper based on their requirements to be performed. The dominant sources of error, measured via fidelity, are written for each gate. Furthermore, we provide the infidelity scaling for the most dominant error factor. For the magnetic dipolar gate, the infidelity scaling $O(r^3)$ is valid if the direct interaction during activation can be ignored (see Section V for more details). A comparison between achievable fidelities and corresponding gate times of these gates is shown in Figure 8.

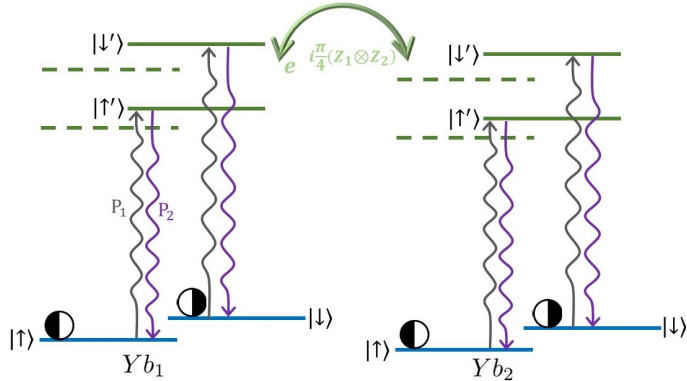


FIG. 2. Diagram of the magnetic dipolar gate mechanism. The pulse sequence for executing a magnetic dipolar-based phase gate between nearby Yb ions begins with preparing a superposition of passive qubit states indicated by half-black coloured circles. The population is then transferred to the excited state using four simultaneous π pulses, denoted by P_1 . A two-qubit phase gate is applied through electronic magnetic dipolar interaction. After a time delay, the population is returned to the ground state using another set of π pulses, denoted by P_2 .

B. Photon scattering gate scheme

Scattering a single photon from the qubit-cavity system can be used to perform a controlled phase-flip gate between qubits [57, 59]. This method has been experimentally realized as a locally controlled phase-flip gate with neutral atoms [60] and has been theoretically explored for non-local controlled phase gates between rare-earth ions in separate microsphere cavities [61]. While these studies focus on the strong coupling regime, Ref [49] extends the approach to implement a CZ gate between two qubits and provides a fidelity expression applicable to both weak and strong coupling regimes.

This scheme requires the detection of a single photon. Alternatively, it can be adapted for quantum non-demolition (QND) measurements to detect the presence of the photon without measuring or destroying its quantum state by probing the quantum emitter system [62].

For this scheme, we employ two of the ground state hyperfine levels of Yb ions as qubit levels ($|\uparrow\rangle$ and $|\downarrow\rangle$), while the first hyperfine level in the excited state serves as an ancillary level ($|\uparrow'\rangle$). The interaction between two Yb ions is mediated by scattering a single photon (in the state $|P\rangle$) from a single-

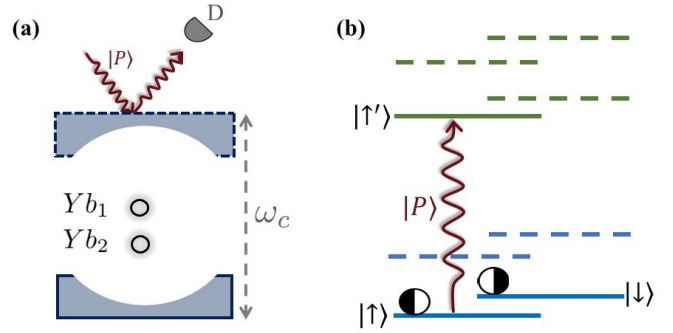


FIG. 3. (a) Schematic of the photon-scattering gate scheme setup. (b) The pertinent hyperfine energy level structure of the Yb ions and the coupling configuration, where the $|\uparrow\rangle \leftrightarrow |\uparrow'\rangle$ transitions of both Yb ions are resonant with each other and with the cavity mode ω_c .

sided cavity containing the Yb ions, as illustrated in Figure 3. We tune the $|\uparrow\rangle \leftrightarrow |\uparrow'\rangle$ transition of the ions to resonance with each other and with the cavity. If both qubits are in the state $|\downarrow\rangle$, the photon enters the cavity, reflects off its interior, and exits, resulting in a π -phase shift in the joint ion-photon state. Conversely, if either or both qubits are in the state $|\uparrow\rangle$, the cavity mode is altered, preventing the photon from entering, and the photon is instead reflected off the cavity's out-coupling mirror. Therefore, a photon detector (denoted by D in Figure 3) can herald the CZ gate. The unitary operator describing this scheme is given with $\text{CZ}^{(2)} = \exp(i\pi|\downarrow\downarrow\rangle\langle\downarrow\downarrow| \otimes |P\rangle\langle P|)$. A CNOT gate is achieved by post-selecting the state of the photon and conjugated by Hadamard gates on the target qubit.

C. Photon interference-based gate scheme

This scheme, originally introduced by Barrett and Kok in [58], is a non-deterministic entanglement generation protocol that can be applied in designing quantum network elements. [47, 53, 63, 64]. While initially developed without a cavity, applying remote cavities to host each individual ion can significantly enhance the fidelity of the scheme (see Section V C for more details). This entanglement generation protocol can be adapted into a CZ gate by measuring the photons in the mutually unbiased basis (MUB) instead of the photon number basis [65].

For this scheme, a three-level system is required, consisting of two qubit levels in the ground state hyperfine manifold,

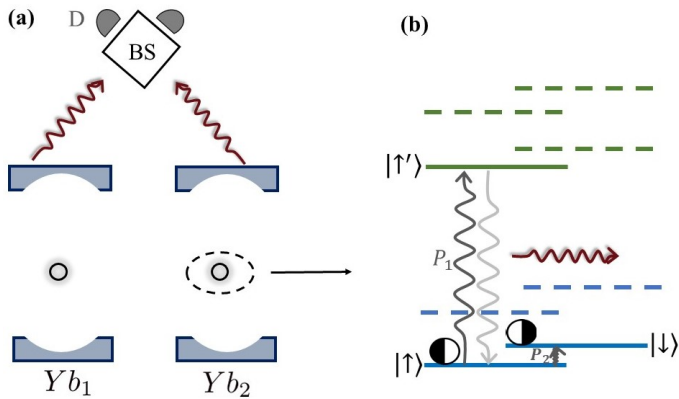


FIG. 4. (a) Schematic of the photon interference-based gate scheme setup: Each Yb ion is positioned within a cavity. The spontaneously emitted photons are routed to a 50:50 beam splitter for detection. (b) To execute the gate, a pulse P_1 , tuned to resonance with the $|\uparrow\rangle \mapsto |\uparrow'\rangle$ transition, drives the Yb ions into their excited state. Next, a microwave π pulse P_2 , is applied to flip the qubit states (details are discussed in the main text). Subsequently, a second optical excitation is applied using the P_1 pulse.

denoted by $|\uparrow\rangle$ and $|\downarrow\rangle$, and an ancillary excited state level, denoted by $|\uparrow'\rangle$, as illustrated in Figure 4. Initially, both ions are pumped into the $|\uparrow\rangle$ level. Then, by applying a microwave $\pi/2$ pulse to each ion, a superposition of $(|\uparrow\rangle + |\downarrow\rangle)/\sqrt{2}$ is created. Next, an optical π pulse is applied in resonance with the $|\uparrow\rangle \mapsto |\uparrow'\rangle$ transition for each ion. The excited states will eventually decay (with potential enhancement from Purcell effects when ions are placed in cavities), creating entanglement between the qubit state and the photon number. This results in the state $(|\uparrow 1\rangle + |\downarrow 0\rangle)/\sqrt{2}$, where 1(0) indicates the presence (absence) of a photon. The emitted photon(s) are then sent to a beam splitter (BS) positioned midway between the ions, where the which-path information is erased before the photon detection event occurs. Detection of a single photon will project the joint state of the two ions into a maximally entangled state. However, there is a possibility that both ions were excited and emitted photons, but one of the photons was lost during transmission. To rule out this scenario, which would result in a product state rather than a Bell state, a π microwave pulse (pulse P_2 in Figure 4) is applied to the ground state levels right after the first excitation-emission step, causing a spin flip. This is followed by a second round of optical excitation. Detecting two sequential single photons ensures that the remote Yb ions are in an entangled Bell state

$$|\psi_{\pm}\rangle = \frac{1}{\sqrt{2}}(|\uparrow_{Yb_1}\downarrow_{Yb_2}\rangle \pm |\downarrow_{Yb_1}\uparrow_{Yb_2}\rangle), \quad (3)$$

where $+$ ($-$) sign indicates the case such that the same (different) detector(s) registered a photon. It can be shown that by altering the measurement basis, this scheme can be transformed into a CZ gate (see Section SV for the derivation).

IV. FIDELITY COMPUTATION

In this section, with a focus on quantum networks applications, we introduce a perturbative approach to compute the state fidelity—the distance between an output state produced by the imperfect gate to an output state produced by the ideal implementation of the gate, given a specific input state. Later, in Section SIII, we demonstrate how our approach can be utilized for the computation of the entanglement fidelity and the average fidelity of a gate which are common measures of the overall performance of a gate scheme [4] with a general use case in quantum computing tasks. These results provide a basis for estimating errors in single- and two-qubit operations.

From this point forward, ‘fidelity’ refers to state fidelity unless explicitly stated otherwise to indicate average gate fidelity.

To quantify the state fidelity of a two-qubit gate, we use tools from time-dependent perturbation theory to analytically derive expressions for the lowest-order non-zero error contributions, which for many realistic applications is sufficient to infer the quality of the gate. We model the noisy gate as a Markovian evolution, which allows us to exploit the Gorini, Kossakowski, Lindblad and Sudarshan (GKLS) master equation to describe the gate dynamics. It is worth noting that this approach works for any initial state. To compare our method with the prior literature, we highlight that the previous works [49, 53] have focused on solving the master equations to obtain output state fidelities, which can be challenging, particularly as the system size increases. To clarify, denoting the Hilbert space dimension by d (for our purposes d gets as large as 16), our method only requires matrix multiplications of size d , and has a complexity of $O(d^3)$ with system size. In contrast, previous approaches necessitate the exponentiation of an operator of size d^2 , representing the noisy Lindbladian superoperator, which translates to $O(d^6)$ computational complexity.

In deriving expressions for the dominant error terms, we consider that imperfections may arise in three different ways: (1) Hermitian perturbations to the gate Hamiltonian, (2) weak Markovian decoherence due to irreversible processes captured by standard Lindblad collapse operators, and (3) non-Hermitian perturbations to the ideal gate Hamiltonian. The first error process gives rise to errors that maintain state coherence and could be eliminated through improved quantum characterization and control. The second error process captures the competition between the desired quantum evolution of the system and its direct interaction with the environment. The third error process can arise due to a combination of the previous two in an analytically simplified model. This latter process is useful for capturing dispersive interactions in the presence of environmental noise, such as in the virtual photon exchange gate [49] (we refer the reader to Section SVII for the details).

Consider that the desired gate is implemented by a gate Hamiltonian denoted by $H_g(t)$. We assume that this Hamiltonian produces a unitary propagator $U_g(T_g, 0) = \mathcal{T} \exp(-\frac{i}{\hbar} \int_0^{T_g} H_g(t) dt)$ that evolves the quantum system state $|\psi(t)\rangle$ from time $t = 0$ to some finite gate time T_g , at which

time the state $|\psi(T_g)\rangle$ is the ideal result of the gate i.e., the solution to the Schrödinger equation

$$\frac{d}{dt}|\psi(t)\rangle = -\frac{i}{\hbar}H_g(t)|\psi(t)\rangle. \quad (4)$$

Due to the presence of imperfections, we consider that the actual evolution of the quantum state is governed by a master equation of the form $\frac{d}{dt}\rho = \mathcal{L}\rho$ for a Lindbladian superoperator \mathcal{L} that is defined by

$$\mathcal{L} = -\frac{i}{\hbar}\mathcal{H} + \sum_k \gamma_k \mathcal{D}(L_k). \quad (5)$$

where $\mathcal{H}\rho = H(t)\rho - \rho H^\dagger(t)$ is the Hamiltonian superoperator corresponding to Hamiltonian $H(t) = H_g(t) + \delta\tilde{H}_e(t)$ for a possibly non-Hermitian perturbation $\tilde{H}_e(t)$ with weight δ . Direct irreversible errors are captured by the dissipative superoperator $\mathcal{D}(L) = L\rho L^\dagger - \frac{1}{2}\{L^\dagger L, \rho\}$ for all relevant Lindblad collapse operators L_k with associated rate γ_k .

To simplify the analysis, we make the assumption that the gate time T_g is characterized well and can be implemented with enough precision so that the actual output state is well-approximated by $\rho(T_g)$. That is, we assume errors arising due to other factors will dominate any small differences between $\rho(t)$ and $\rho(T_g)$ when $t \simeq T_g$. In that case, the fidelity F of the actual output state $\rho(T_g)$ with respect to the ideal state $|\psi(T_g)\rangle$ is then given by

$$F = \langle \psi(T_g) | \rho(T_g) | \psi(T_g) \rangle \quad (6)$$

and we define the corresponding error as $\varepsilon = 1 - F$. Note that the assumption on $t \simeq T_g$ can be relaxed but the result is a more complicated expression that is less intuitive.

Using time-dependent perturbation theory (see Section SI), we find that the error can be expanded into

$$\varepsilon = \varepsilon_L^{(1)} + \varepsilon_H^{(1)} + \varepsilon_{HH}^{(2)} + \varepsilon_{LH}^{(2)} + \varepsilon_{LL}^{(2)} + \dots \quad (7)$$

where the superscript (n) indicates the n -th order perturbation to $\varepsilon^{(0)} = 0$ and the subscripts H and L indicate whether the term arises due to perturbations of H and irreversible processes captured by L_k , respectively. The first-order terms are given by

$$\varepsilon_L^{(1)} = \sum_k \int_0^{T_g} \gamma_k \left(\langle L_k^\dagger(t) L_k(t) \rangle - |\langle L_k(t) \rangle|^2 \right) dt \quad (8)$$

$$\varepsilon_H^{(1)} = -\frac{2\delta}{\hbar} \int_0^{T_g} \text{Im}(\langle \tilde{H}_e(t) \rangle) dt. \quad (9)$$

Here, we have employed the convention that $\langle \mathcal{O}(t) \rangle = \langle \psi(t) | \mathcal{O} | \psi(t) \rangle$ for an operator \mathcal{O} .

An interesting consequence of the first-order result is that $\varepsilon_H^{(1)}$ vanishes if \tilde{H}_e is Hermitian. To obtain the first non-zero term arising from reversible errors (Hermitian perturbations to H_g), it is necessary to go to the second-order terms. However, since $\varepsilon_L^{(1)}$ is generally non-zero at the first order, it will tend to dominate over $\varepsilon_{HL}^{(2)}$ and $\varepsilon_{LL}^{(2)}$. The expressions for these

two terms are presented in the Section SI for an interested reader. Here, out of second order terms, we only focus on the reversible error $\varepsilon_{HH}^{(2)}$ due to the Hermitian perturbation $H_e = (\tilde{H}_e + \tilde{H}_e^\dagger)/2$, which can be non-zero even in the absence of irreversible errors and is given by

$$\varepsilon_{HH}^{(2)} = \frac{2\delta^2}{\hbar^2} \int_0^{T_g} \int_0^t \text{Re}(\langle H_e(t) H_e(t') \rangle - \langle H_e(t) \rangle \langle H_e(t') \rangle) dt dt', \quad (10)$$

where the two-time correlation is computed by $\langle \mathcal{O}_1(t) \mathcal{O}_2(t') \rangle = \langle \psi(t) | \mathcal{O}_1 U_g(t, t') \mathcal{O}_2 | \psi(t') \rangle$ for any pair of operators $\mathcal{O}_1, \mathcal{O}_2$.

For the three expressions obtained for $\varepsilon_L^{(1)}$, $\varepsilon_H^{(1)}$ and $\varepsilon_{HH}^{(2)}$ to be evaluated analytically it is necessary to obtain an analytic solution to the ideal gate evolution. If the integrals can also be computed analytically, we will have a full analytical expression. However, in case the integrals cannot be computed analytically, one can utilize numerical methods to compute the infidelities for a fixed gate time T_g in terms of the imperfection parameters (i.e., δ and γ_k). This is generally much easier than solving the full system master equation to obtain the exact fidelity.

In the following, we use this method to compute the state fidelity of the magnetic dipolar gate, which serves as an example of having a Hermitian error Hamiltonian. Additionally, in Section SVII, we re-compute the state fidelity of the virtual photon exchange gate [49] as an example of a non-Hermitian perturbation Hamiltonian. However, this gate and its fidelity calculation have already been discussed in [49, 53, 66].

V. FIDELITY ESTIMATIONS AND IMPLEMENTATIONS

In this section, we provide a detailed analysis of the state fidelity expressions for each gate scheme, using both analytical and numerical techniques to evaluate their performance for quantum networks purposes. We also discuss the requirements for the experimental implementation of the parameters involved in the fidelity expressions. Based on these results, we estimate the achievable fidelity of each gate scheme for individual Yb ions at the current state of technology.

A. Magnetic dipolar gate

Employing the perturbative method, which was described in the previous section, allows us to compute the state fidelity of the magnetic dipole-dipole interaction gate as (see Section SIII for the derivation)

$$\begin{aligned} F_{\text{MD}} = & 1 - T_{\text{act}} \left(\frac{7}{8}(\gamma_{1,\uparrow'} + \gamma_{1,\downarrow'}) + \frac{13}{16}(\gamma_2 + \gamma_3) + \frac{1}{2}(\gamma_4 + \gamma_5) \right) \\ & - T_{\text{int}} \left(\gamma_{1,\uparrow'} + \gamma_{1,\downarrow'} + \frac{3}{4}\gamma_3 + \frac{1}{2}\gamma_5 \right) - \frac{a(J_x + J_y)^2}{J_z^2}, \end{aligned} \quad (11)$$

where $T_{act} = \frac{\pi}{\Omega}$ represents the activation time, the duration needed to transfer the population from passive to active qubits, with Ω being the Rabi frequency. Here the dissipative parameters affecting the system are considered as optical decay rate $\gamma_{1,\uparrow'} (\gamma_{1,\downarrow'})$ corresponding to the transitions $|\uparrow'\rangle: |\uparrow\rangle \rightarrow |\downarrow'\rangle: |\downarrow\rangle$, ground (excited) state spin decay rate $\gamma_{2(3)}$, and ground (excited) state spin dephase rate $\gamma_{4(5)}$. The interaction time between two active qubits in the excited states is denoted by $T_{int} = \frac{\hbar\pi}{4J_z}$ where $J_z = \frac{\mu_0(\mu_B g_z)^2}{8\pi r^3}$ is the coupling strength between the qubits, with μ_0 being the vacuum permeability, μ_B the Bohr magneton, g_z as the principal value of the g-tensor, and r the spatial distance between two Yb ions. In this analysis $J_i = \frac{\mu_0(\mu_B g_i)^2}{16\pi r^3}$ (for $i = x, y$) define the transverse components of the dipolar interaction, where we consider the point symmetry with $g_x = g_y \equiv g_{\perp}$ and $g_z \equiv g_{\parallel}$. Here, a is a coefficient defined by $a = (32(2 - \sqrt{2}) - \pi^2)/64$. For $J_x = J_y \equiv J_{\perp}$ the second order error (denoted by coefficient a) is bounded above by $\sim J_{\perp}^2/J_{\parallel}^2$ which improves the estimation obtained in Ref. [48]. In $^{171}\text{Yb}^{3+}:\text{YVO}$, the excited state g-tensor components parallel and perpendicular to the crystal symmetry axis (the c axis) are $g_{\parallel} = 2.51$ and $g_{\perp} = 1.7$ [17]. This results in a second-order error contribution to the fidelity of approximately 10^{-2} , setting a lower bound for the fidelity. This lower bound is relevant in cases where transverse interactions mediate the gate process.

In modelling the system, we neglect certain mechanisms. Below, we describe how these effects scale relative to the two-qubit process.

Following Ref. [48], we disregard the nuclear magnetic dipolar interaction, as its strength is $\sim 10^7$ times weaker than the electronic magnetic dipolar interaction. This difference arises mostly from the small nuclear magnetic moment (μ_N), and the nuclear g factor ($g_n = 0.987$).

When performing the CNOT gate, some infidelity inevitably arises from the single-qubit rotations. Among the single-qubit gates, the Hadamard gate for example can be performed through $\pi/2$ microwave pulses between hyperfine levels which involves nuclear magneton and results in a long gate time of $T_{\text{single}} = \frac{\hbar\pi}{\mu_N B} \approx 0.13\mu\text{s}$ (at $B = 500$ mT). Conversely, one can couple nuclear levels indirectly through optical pulses. Although this requires two consecutive pulses, it enables a faster gate time of $T_{\text{single}} = \frac{2\hbar\pi}{\mu_B B} \approx 0.14\text{ns}$ [48].

Ref. [48] discusses that the intrinsic optical decoherence rate causes the infidelity $\sim T_{\text{single}}/T_{2o}$, with T_{2o} being the optical coherence time. Plugging in $T_{2o} = 91\mu\text{s}$ (at $B = 500$ mT) [17], we get an infidelity of about $\epsilon_{\text{single}} \simeq 1.5 \times 10^{-6}$. Therefore, in these analyses, we assume that the fidelity of the CNOT gate is primarily determined by the two-qubit gate processes. However, we include these fast excitations in our analysis to capture their effect on the two-qubit activation process (see the second term in Equation (11)).

Moreover, the error corresponding to off-resonant excitations due to optical π pulses (involved in both single-qubit and activation operations) cause infidelity of $\sim \exp\left(-\frac{\pi}{2} \left(\frac{\Delta_s}{\Omega}\right)^2\right)$ with Δ_s being the hyperfine splitting [48]. To avoid any off-

resonance excitation, the Rabi frequency of the activation pulses should be much smaller than the smallest hyperfine splitting, and hence, choosing $\Delta_s \geq 10\Omega$ yields an insignificant infidelity of $\sim 10^{-68}$. For example for a splitting of ~ 100 MHz, a Rabi frequency of at most 10 MHz is required. Employing this Rabi frequency to apply four simultaneous π -pulses results in an activation process to take approximately $T_{act} = \frac{\pi}{\Omega} \sim 0.31\mu\text{s}$.

If the splitting is small, achieving fast excitations can be challenging. In that case, one should examine how close the ions have to be to obtain decent fidelities. Therefore, there is a trade-off between splitting and separation of ions. In Figure 5, we demonstrate fidelity as a function of Rabi frequency and ions' separation illustrating the variation in laser power corresponding to the changing distance between two ions.

We note that Equation (11), and hence the $1 - O(r^3)$ fidelity scaling, is obtained under the assumption that direct interaction is negligible during excitations. More formally, we assume $\|H_{\text{int}}T_{act}\| \ll 1$ with H_{int} being the dipolar interaction Hamiltonian. However, when considering $\Omega = 10\text{MHz}$, the numerical simulation of the Yb system shows that this assumption breaks down at small separations with a turning point around $r \sim 5$ nm. Therefore, for Yb ions, we anticipate the highest fidelity around this separation. See Section SIII and Figure S2 for more details. For $r > 5$ nm, as Figure 5 confirms, the distance cannot be arbitrarily large, as the fidelity of the two-qubit process decreases with increased separation. Two nearby ions can be found by implanting each ion at precise locations within the crystal, achieving a separation of just a few nanometers between them [67].

To limit the decay process, we choose two of the lowest ground state hyperfine levels with long enough coherence time as the passive qubit levels. Furthermore, in $^{171}\text{Yb}^{3+}:\text{YVO}$ system with a nonzero perpendicular component of the g-tensor ($g_{\perp} \neq 0$), choosing opposite nuclear levels within each electronic doublet reduces spin flip-flop errors during the two-qubit gate process [48]. This approach offers two options for selecting active qubits within both different electron spin and nuclear spins (e.g., both solid or dashed green lines in Figure 2).

The optical decay rate for an ensemble of $^{171}\text{Yb}^{3+}:\text{YVO}$ is $\gamma_{1,\downarrow'} \simeq \gamma_{1,\uparrow'} \equiv \gamma_1 = 2\pi \times 596$ Hz [17]. We estimate the ground state spin dephasing rate with relation $\gamma_4 = 1/T_{2s,g} - \gamma_2/2 \simeq 2\pi \times 3.6$ Hz, where $T_{2s,g} = 6.6$ ms (at $B = 440$ mT) is the ground state spin coherence time [17]. For single $^{171}\text{Yb}^{3+}$ ions coupled to a YVO photonic crystal cavity, the ground state spin coherence time is extended to 31 ms using Carr-Purcell Meiboom-Gill (CPMG) decoupling sequences and the ground state spin decay rate and is measured to be $\gamma_2 = 2\pi \times 2.95$ Hz [31]. Similarly, we estimate the excited state spin dephasing rate with relation $\gamma_5 = 1/T_{2s,e} - \gamma_3/2 = 2\pi \times 4.5$ KHz, where $T_{2s,e}$ is the excited state spin coherence time, measured to be $35\mu\text{s}$ at low magnetic fields [26]. We assume that the excited state spin decay rate (γ_3) is the same as the ground state (γ_2), as there is no available information on this to the best of our knowledge. Therefore, the fidelities of 0.95 and 0.9 can be achieved for

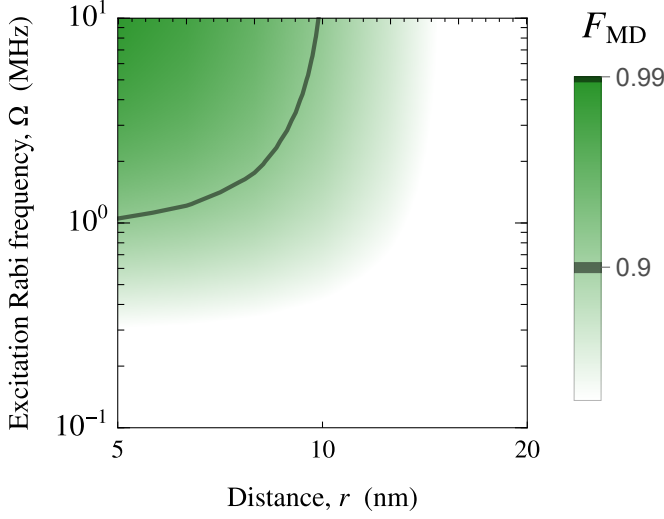


FIG. 5. Fidelity of the magnetic dipolar gate as a function of Rabi frequency (activation pulse) and the distance between two Yb ions doped into YVO crystal. If two ions are spatially far away more than 10 nm, fast excitations may still achieve a fidelity of above 90% for the magnetic dipolar gate. Here, we start the plot at 5 nm, where modelling the system through the perturbation method (i.e., Equation (11)) matches the exact simulation of the system (see Figure S2 for more details).

distances $r = 5$ nm, and $r = 10$ nm respectively. The overall gate time is defined to be $T_{g,MD} = 2T_{act} + T_{int}$, where the coefficient 2 is considered for activation and deactivation pulses. The corresponding gate times for distances $r = 5$ nm, and $r = 10$ nm are $1\mu\text{s}$, and $3.68\mu\text{s}$ respectively.

B. Photon scattering gate

In this scheme, photon loss due to spontaneous emission, scattering, detector efficiency and other deficiencies make the gate operation probabilistic. However, they do not cause errors as long as the photon count is properly recorded [57]. Therefore, we assume that the photon is successfully detected and focus on the remaining sources of error that impact the fidelity. The fidelity of the photon-scattering gate scheme in high cooperativity regime $C \gg 1$ is computed in [49] to be

$$F_{PS} = 1 - \frac{5}{2C} - \frac{(\delta_p^2 + \sigma_p^2)}{4\gamma_1^2 C^2} (11 - 80\alpha^2 + 192\alpha^4) - \frac{(\delta_{Yb_1} - \delta_{Yb_2})^2}{2\gamma_1^2 C} - \Gamma T_{g,PS}, \quad (12)$$

where δ_p is the cavity-photon detuning, δ_{Yb_n} denotes the detuning of the cavity frequency from the optical transition of the n^{th} system, σ_p is the spectral standard deviation of the incident photon that is modelled assuming a Gaussian wave packet for the photon, Γ represents the effective decoherence

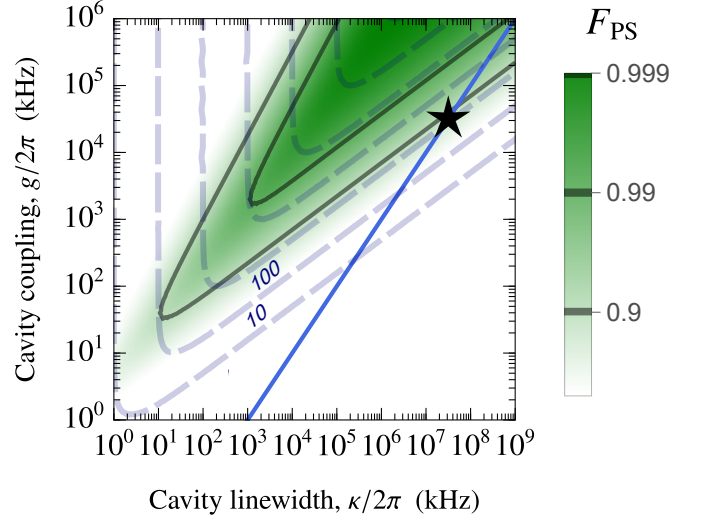


FIG. 6. Fidelity of the photon scattering gate as a function of cavity parameters. The dashed lines represent the necessary maximum Purcell enhancement (when on resonance) for each regime, increasing exponentially by powers of ten ($10, 10^2, 10^3$, and so on). Here we assume $\delta_p = \delta_{Yb_1} - \delta_{Yb_2} = 0$. The cavity coupling and decay rates set to $g = 2\pi \times 23$ MHz, and $\kappa = 2\pi \times 30.7$ GHz [31]. Since the presence of a cavity can negatively impact the optical coherence, we use a slightly reduced coherence time of $39\mu\text{s}$ compared to the bulk value of $91\mu\text{s}$ (at $B = 500\text{mT}$) [17] prior to accounting for Purcell enhancement, which we estimated from Ref. [31]. The star mark indicates the current achievable fidelity of this scheme for Yb:YVO to be 0.8. The realistic parameter regimes achievable by a physical device are expected to center around the star mark (reflecting current implementations), whereas reaching the strong coupling regime remains highly challenging. The blue line indicates the current ratio $\alpha = g/\kappa$ and is studied separately in Figure 9.

rate, and $T_{g,PS}$ is the gate time. The parameter $\alpha = g/\kappa$ defines the ratio between the cavity-ion coupling rate g , and the cavity decay rate κ and the cavity cooperativity is $C = 4g^2/\kappa\gamma_1$.

While the analytical expression for gate fidelity has been previously derived, it does not account for optical pure dephasing and spin decoherence effects. To address these limitations, we approach the problem using a fully numerical method based on input-output theory (see Section SVI). However, in our numerical simulation, we consider the photon to have a Lorentzian spectrum rather than the Gaussian spectrum used in the analytic expression since otherwise a large time-dependent master equation must be solved that substantially increases simulation time and restricts the parameter range that we can explore. Thus, although the qualitative behaviour and scaling properties are expected to be the same as in Equation (12), quantitative comparisons require caution.

In Figure 6, we display our fidelity estimations as a func-

tion of cavity parameters (g, κ) using the numerical simulation where we consider a photon with a Lorentzian-shaped spectrum. We also use this numerical simulation to validate properties of the previous analytical approximation derived in Equation (12). Our numerical simulation reveals that this analytic expression can be modified to capture the degrading effect of optical pure dephasing when $\alpha \ll 1$ by replacing the cavity cooperativity with an effective cavity cooperativity $C_{eff} = C/(1 + w(T_{1o}/T_{2o} - 1))$, where $w \simeq 0.7$, T_{1o} is the optical lifetime, and T_{2o} is the optical coherence time. Additionally, we find that $\Gamma \propto 1/T_{2s,g}$, where $T_{2s,g}$ represents the ground state spin coherence time, offers a reliable estimate of the error caused by spin decoherence. The exact proportionality coefficient, however, depends on the shape of the photon. When using the same definition of gate time as in [49] along with $\sigma_p = 1/T_{1p}$ where T_{1p} is the scattered photon lifetime, we find $\Gamma \simeq 1/T_{2s,g}$ quantitatively agrees with the numerical simulation.

The numerical simulation also leads us to identify a previously-overlooked alteration of the lower-bound error scaling when spin decoherence is non-negligible. Assuming $\delta_p = 0$ and the ions are in perfect resonance with each other and with the cavity, from Equation (12), we find that in the absence of spin dephasing ($\Gamma = 0$), it is always possible to reach the minimum error of $1 - F_{PS,max} \propto 1/C$ by scattering a very narrow photon ($\sigma_p \ll 1$). However, the gate time is proportional to the time it takes to scatter the photon ($T_{g,PS} \propto 1/\sigma_p$). Thus, as C is increased to improve fidelity, it is necessary to increase $T_{g,PS}$ and so if $\Gamma \neq 0$ this causes the last term in Equation (12) to increase. This imposes a trade-off between having an error from the spectral broadening (i.e., σ_p^2 term) or from the spin dephasing (i.e., $\Gamma T_{g,PS}$ term). In Ref. [49], this trade-off was explored but assumed to always be of a second-order correction to the seemingly dominant $1/C$ term when the gate time was optimized. This is, in fact, not the case.

For a given cavity cooperativity and spin dephasing rate Γ , there is an optimal bandwidth of the photon that minimizes the error. This optimal bandwidth can be computed by setting the third and the last terms in Equation (12) to be equal. Solving for the bandwidth implies that it must scale as $\sigma_p \propto C^{2/3}$ and hence $\Gamma T_{g,PS} \propto 1/C^{2/3}$. Thus, if either Γ or C is large enough, this scheme will have an error scaling of $1/C^{2/3}$ rather than $1/C$, which is significantly worse for large C .

In addition to setting the photon bandwidth, it is necessary to define a photon truncation time that defines the total gate time (denoted by $T_{g,PS}$). If one stops measuring the photon too soon, there will be low efficiency. On the other hand, if one waits too long, spin decoherence will be exacerbated. For the value of $T_{2s,g}$ expected, we select this additional truncation time to be proportional to the time-scale of the scattered photon and such that it has a minimal impact on the fidelity for the range of cooperativity explored, leading to $T_{g,PS} = 7T_{1p}$ which implies only 0.1% loss.

In our simulations, we numerically optimize the spectral standard deviation (σ_p) to achieve maximum fidelity. We also assume that the gate operation is sufficiently fast for the ions to effectively avoid experiencing spectral diffusion

during this period. However, even for single emitters, spectral diffusion of the optical transition can reduce the Ramsey coherence time [31]. Any remaining spectral diffusion could, in principle, be handled using active feedback or special decoupling techniques. Therefore, we focus on the upper bound fidelity imposed by the measured T_{2o} value only. Although the spectral diffusion can be overcome with additional filtering or time binning, if unmitigated, this effect must be incorporated into the fidelity calculation. Assuming that spectral diffusion primarily determines the detuning between the ions' optical transitions during the gate time, one can approximately account for this by including the time-dependent spectral diffusion function in the fidelity equations via the $\delta_{Yb_1} - \delta_{Yb_2}$ term.

In his scheme, similar to the previous approach, we employ two hyperfine levels in the ground state as qubit levels. However, unlike the previous scheme, only a single hyperfine level in the excited state is required to serve as an auxiliary state. After qubit initialization, the transitions $|\uparrow\rangle \mapsto |\uparrow'\rangle$ of each ion should be brought into resonance with one another and with the cavity mode. A magnetic field gradient can tune the optical transitions of the ions into resonance with each other. On the other hand, to bring the cavity-ion system into resonance, the piezoelectric effect can be employed to adjust the cavity frequency relative to the transition frequency of the ions within it [68]. When bringing the ions into resonance with each other, it should be noted that the laser field can couple both hyperfine qubit levels to the excited state. To avoid this this undesired coupling, the transition $|\downarrow\rangle \mapsto |\uparrow'\rangle$ should be detuned far from the cavity resonance.

Photonic cavities have been fabricated in YVO crystals using ion beam milling, achieving a cavity-Yb ion coupling rate of $g = 2\pi \times 23$ MHz and a cavity decay rate of $\kappa = 2\pi \times 30.7$ GHz [31]. For single Yb ions coupled to this cavity, a reduced optical lifetime of $2.27\mu s$ have been measured [31]. However, the fabrication process poses a significant risk of crystal damage, making it a challenging method. An alternative approach involves designing a hybrid photonic crystal cavity system, where the cavity is fabricated separately and later transferred onto the crystal. For instance, a Gallium Arsenide (GaAs) photonic crystal cavity has been developed, demonstrating a reduced optical lifetime of $4.2\mu s$ corresponding to the Purcell factor of 179 for strongly coupled single Yb ions coupled to hybrid GaAs-YVO system [32].

C. Photon interference-based gate

In this scheme, the fidelity is primarily restricted by the optical quality of the source. Specifically, when transferring to an MUB basis, we assume all single-qubit gates and the beam splitter to be ideal. Therefore, we consider the fidelity of the two-qubit gate to be limited by the two-qubit operation.

This scheme requires the detection of two consecutive single photons. Assuming the detection time (T_d) is longer than

the optical lifetime ($T_d > T_{1o}$) the fidelity is given by [52, 53]

$$F_{PI} = \frac{1}{2} \left(1 + \frac{\gamma_1^2}{(\gamma_1 + 2\gamma^*)^2 + \Delta_\omega^2} \right), \quad (13)$$

where γ_1 represents the optical decay rate from the auxiliary excited state $|\uparrow'\rangle$ to the ground-state qubit level $|\uparrow\rangle$ (assuming the decay rate from $|\uparrow'\rangle \mapsto |\downarrow\rangle$ is negligible), γ^* is the optical pure dephasing rate, and Δ_ω is the detuning between optical transitions of two Yb ions. We estimate the optical pure dephasing rate with relation $\gamma^* = 1/T_{2o} - \gamma_1/2 = 2\pi \times 1.4$ kHz, where $T_{2o} = 91\mu\text{s}$ is the optical coherence time of Yb ions in YVO crystal bulk [17]. This results in a fidelity of $F_{PI} = 0.51$.

This reduced fidelity is attributed to the Yb ion optical pure dephasing rate captured by T_{2o} , which is influenced by both spin decoherence and spectral fluctuations of the optical transition that occur faster than the optical lifetime. However, knowing that the ground state spin coherence time $T_{2s} = 31$ ms [31] is already two orders of magnitude larger than the unenhanced optical lifetime $T_{1o} = 267\mu\text{s}$ [17], the contribution of the ground state spin dephasing to the optical decoherence is negligible. Furthermore, any amount of Purcell enhancement needed to overcome the optical dephasing rate will further reduce the impact of the ground state spin decoherence and hence it can be safely neglected in the analysis.

While this gate scheme does not inherently require a cavity to be performed, below, we discuss how employing a cavity can enhance the fidelity of the gate between two Yb ions. In case of implying a cavity Equation (13) is modified to

$$F'_{PI} = \frac{1}{2} \left(1 + \frac{\gamma_1'^2}{(\gamma_1' + 2\gamma^*)^2 + \Delta_\omega^2} \right), \quad (14)$$

where $\gamma_1' = \gamma_{1r}F_p + \gamma_1$ defines the Purcell-enhanced optical decay rate of the ion in the presence of the cavity, $\gamma_1 = \gamma_{1r} + \gamma_{1nr}$ is Yb ion decay rate with radiative (γ_{1r}) and non-radiative decay rate (γ_{1nr}) parts. The Purcell factor in both strong coupling and bad-cavity regimes is defined as [66]

$$F_p = \frac{R\kappa}{\gamma_r(\kappa + R)}, \quad (15)$$

with κ being the cavity decay rate, and

$$R = \frac{4g^2(\kappa + \gamma_1 + 2\gamma^*)}{(\kappa + \gamma_1 + 2\gamma^*)^2 + 4\Delta_\omega^2}. \quad (16)$$

We demonstrate how the fidelity of this scheme varies with different cavity parameters in Figure 7. Additionally, we determine the necessary Purcell factor for achieving a specific fidelity threshold.

Assuming resonant excitation results in photons with a Lorentzian spectral shape, and since this scheme takes two emissions, we consider the gate time for this scheme twice the gate time definition in the photon scattering gate $T_{g,PI} = 14T'_{1p}$. Therefore, we allow at most $7T'_{1p}$ for each emission time bin. However, it should be noted that here

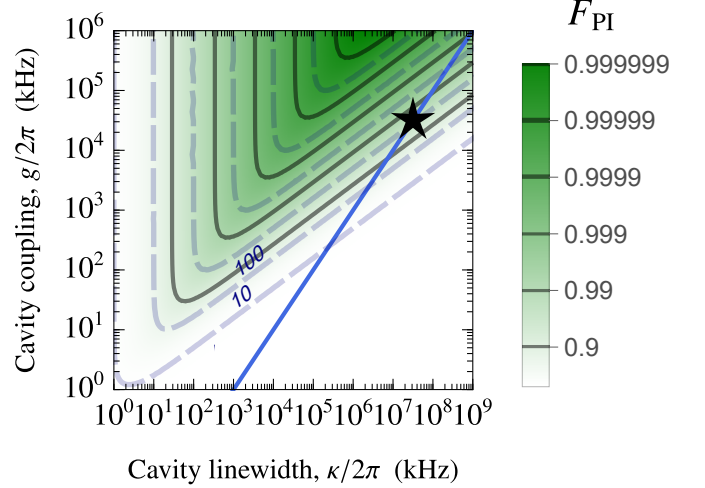


FIG. 7. Fidelity of photon interference scheme as a function of cavity parameters. Here we use a slightly larger pure dephasing rate of $\gamma^* = 2\pi \times 3.8$ kHz compared to bulk, which is expected for ions in a cavity [31] and is consistent with the dephasing rate we considered for the photon scattering scheme. We also assume that spectral diffusion is mitigated, so the optical transition frequencies of the Yb ions are in perfect resonance with each other, i.e., $\Delta_\omega = 0$ (see Section V B for more information). With these assumptions, the current experimental parameters reach a fidelity of 0.95, which is indicated by the star symbol. The blue line is studied separately in Figure 9.

T'_{1p} denotes the Purcell-enhanced lifetime of the photon set by the emitter while in photon scattering scheme, the photon originates from an external source and not the ion. Furthermore, this gate time neglects the time taken to perform the necessary spin-flip operation between the emission events. However, as discussed in Section V A we assume that single-qubit operations can be implemented much faster than the time it takes to emit two photons.

In this scheme, as in the photon scattering scheme, qubit levels are defined using two of the lowest hyperfine levels in the ground state, along with an ancillary level in the excited state.

VI. TWO-QUBIT GATE SCHEME COMPARISON

In our comparison of gate schemes, we focus on the two-qubit interaction, assuming that within each scheme the single-qubit gate errors are negligible. Nevertheless, we recall that the magnetic dipolar gate requires two additional single-qubit Z gates, and the photon interference scheme requires a measurement basis change to achieve a CZ gate, whereas the photon scattering gate implements it directly.

We now analyze all three two-qubit gate schemes, among which the magnetic dipolar gate is fully deterministic, the photon scattering gate is near deterministic, and the photon

interference-based scheme is a probabilistic scheme with a maximum success probability of 50%.

We begin our comparison with a number of qualitative remarks. In terms of experimentally controlling the energy levels, the magnetic dipolar gate requires two energy levels in both ground and excited states while photon scattering and photon interference-based can be performed utilizing only two energy levels in the ground and one auxiliary level in the excited state. Among the gates, since dipolar-type gates require direct interactions between the qubits (ions), they are highly limited by the spatial separation between the individual ions and hence, the effectiveness of the magnetic dipolar gate falls off significantly if the distance exceeds a few nanometers. At such small distances, the spatial addressability of individual ions is a challenge. Conversely, cavity-based gates have the advantage of being less sensitive to ion separation, enabling operation over distances comparable to the cavity dimensions. However, designing such gates can be challenging due to the difficulty in fabricating nanophotonic crystal cavities, which are limited by the availability of high-quality thin films. Additionally, bringing optical transitions into resonance—with each other and the cavity mode in photon scattering schemes—requires more advanced experimental techniques. The photon interference-based scheme offers greater flexibility in terms of separation distance, as it does not rely on direct qubit-qubit interactions. For instance, a cavityless version of the photon interference-based gate scheme has been successfully implemented between two NV centers separated by 3 meters [69]. While the photon interference-based gate can also be operated without a cavity, incorporating a cavity for rare-earth ions enhances fidelity through Purcell enhancement.

For a quantitative comparison of the gates, we present the fidelities and associated gate times in Figure 8. The symbols in Figure 8 indicate that within a specific gate scheme, a shorter gate time is associated with higher fidelity. However, achieving both shorter gate time and higher fidelity requires either smaller ion separation for the magnetic dipolar scheme or higher cooperativity for the photon scattering and photon interference-based schemes which pose practical restrictions. Nonetheless, the specific cooperativity requirements are scheme-dependent. A comparison between different schemes demonstrates that the photon interference-based scheme achieves superior fidelity and shorter gate times than the photon scattering scheme across both lower (e.g., $C = 100$) and higher (e.g., $C = 1000$) cooperativity regimes. The role of cooperativity in determining the performance of different cavity-based schemes is examined in more detail in Figure 9.

Also, for the distances considered here, the magnetic dipolar gate achieves shorter gate times than the other two schemes. However, attaining high fidelities remains challenging compared to the photon interference-based scheme at cooperativity of $C = 1000$.

The limiting parameter for cavity-based gate schemes is currently achievable cavity cooperativity. Therefore, in Fig-

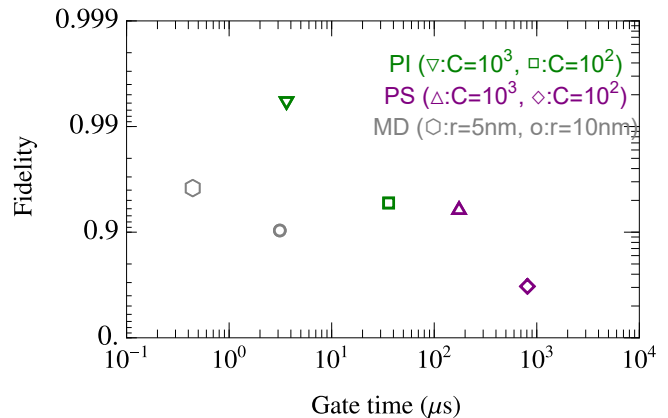


FIG. 8. The fidelities and corresponding gate times of the gate schemes discussed in this work. Here, we present two achievable values for the fidelity and gate time of each scheme, based on experimentally attainable parameters for rare-earth ions. This includes varying the ion separation distance (r) for the magnetic dipolar gate and the cavity cooperativity (C) for the other schemes.

ure 9 we compare the performance of the cavity-based gate schemes in terms of required cooperativity. The photon interference-based scheme is more applicable than the photon scattering scheme with the currently reported cavity cooperativity for Yb to implement a two-qubit gate. To summarize the cooperativity dependence of the different gate schemes, Figure 9 shows that the infidelity of the photon interference-based gate scales as $1/C$, while for the photon scattering scheme, the infidelity scales as $1/C^{2/3}$. For instance, with a cavity cooperativity of 100, the gate errors for the photon interference-based and photon scattering gate schemes are approximately 1% and 4.6% respectively.

VII. CONCLUSION AND OUTLOOK

In this paper, we discussed three particularly attractive two-qubit gate schemes—arguably the most promising choices—given the current state of the art of the technology of the Yb:YVO system, including a deterministic approach, namely magnetic dipolar gate, a near deterministic approach, namely photon scattering scheme and a probabilistic scheme based on photon interference. We introduced a new approach for calculating the state and gate fidelities of a desired gate scheme. With a focus on state fidelity for quantum communication use cases, we examined their feasibility for implementation and compared their performance based on state-of-the-art technology.

Our analysis showed that each gate scheme has its advantages and limitations. The photon interference-based scheme outperforms the photon scattering gate by offering higher fidelity and shorter gate times as cooperativity increases. However, the photon interference-based scheme operates probabilistically, whereas the photon scattering scheme is nearly deterministic. In contrast, the magnetic dipolar gate

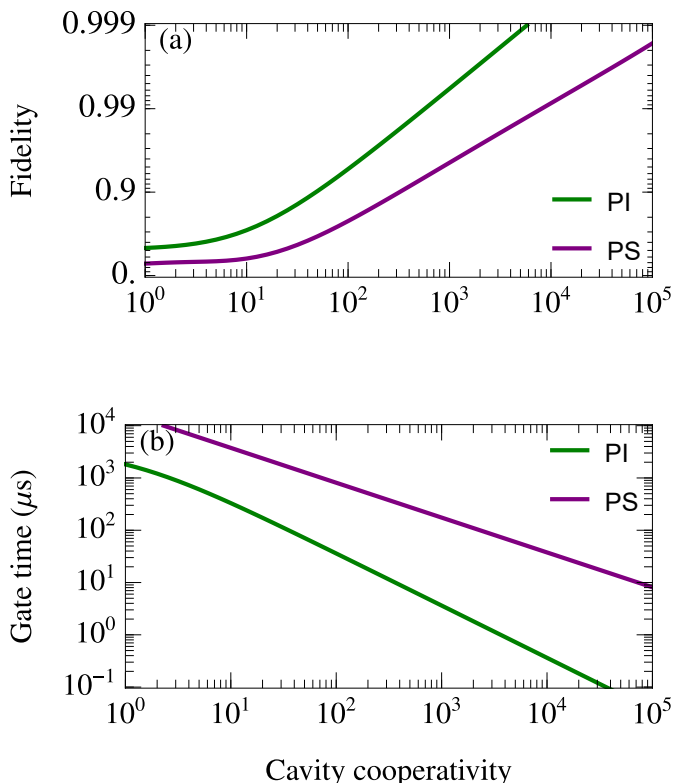


FIG. 9. (a) Fidelity and (b) gate time of the cavity-based gate schemes as a function of cavity cooperativity for a slice of the 2D plots corresponding to $g/\kappa \simeq 0.001$ that intersects with the star marks in Figure 6 and Figure 7.

performs independently of a cavity, making it a promising alternative. However, it relies on tightly localized ions to achieve fast and high-fidelity operations.

To provide a broader perspective, we highlight other potential gate implementation techniques that experimentalists might find valuable, depending on their experimental facilities and specific needs. For example, an alternative approach for implementing a deterministic two-qubit gate involves virtual photon exchange within a cavity [49]. This scheme has

been widely used as a readout protocol in superconducting qubits [70, 71]. Applying it to rare-earth ions requires a high-cooperativity cavity [53]. In Section SVII, we re-calculate the fidelity of this scheme. This example illustrates a scenario involving a non-Hermitian error Hamiltonian, which we analyze using the perturbative method developed in this work. With current technology and in the absence of excited state spin dephasing, this scheme achieves a fidelity of 50%. However, as demonstrated in [53, 66], monitoring the cavity emission can enhance the fidelity of this gate scheme through the post-selection of successful gates, though this comes at the cost of rendering the scheme non-deterministic.

Another scheme of interest for optically long-lived rare-earth ions is introduced in [72]. They demonstrated that the photon interference-based scheme discussed earlier can be modified to become nearly deterministic by incorporating feedback during the measurement process.

Looking forward, one can leverage the optimal gate protocol established in this work for designing a quantum repeater between individual Yb ions and also for distributed quantum computing tasks.

While this work focuses on YVO, it is worth noting that similar approaches presented here could also be applied to other crystals, such as YSO, if a nanophotonic cavity can be designed for $^{171}\text{Yb}^{3+}$: YSO to assess the performance of cavity-based gate schemes.

Although our comparison study targets $^{171}\text{Yb}^{3+}$: YVO system, similar gate comparisons could also be done for other systems (other RE ions in solids, other kinds of defect centers etc.), where the most favourable gates will likely depend on the system parameters such as radiative lifetimes and coherence times as well as the experimental state of the art, e.g. for defect localization and cavity cooperativity.

ACKNOWLEDGEMENT

This work is funded by the NSERC Alliance quantum consortia grants ARAQNE and QUINT and the NRC High-throughput Secure Networks (HTSN) challenge program. We thank Andrei Faraon, Mikael Afzelius, Arsalan Motamedi, Jiawei Ji, Nasser Gohari Kamel and Andrei Ruskuc for useful discussions.

[1] T. Jennewein, G. Weihs, J.-W. Pan, and A. Zeilinger, *Physical review letters* **88**, 017903 (2001).
 [2] N. Sangouard, C. Simon, H. De Riedmatten, and N. Gisin, *Reviews of Modern Physics* **83**, 33 (2011).
 [3] D. E. Deutsch, *Proceedings of the royal society of London. A. mathematical and physical sciences* **425**, 73 (1989).
 [4] M. A. Nielsen and I. L. Chuang, *Phys. Today* **54**, 60 (2001).
 [5] A. Y. Kitaev, A. Shen, and M. N. Vyalyi, *Classical and quantum computation*, 47 (American Mathematical Soc., 2002).
 [6] M. H. Devoret and R. J. Schoelkopf, *Science* **339**, 1169 (2013).

[7] D. Loss and D. P. DiVincenzo, *Physical Review A* **57**, 120 (1998).
 [8] A. Kinos, D. Hunger, R. Kolesov, K. Mølmer, H. de Riedmatten, P. Goldner, A. Tallaire, L. Morvan, P. Berger, S. Welinski, et al., *arXiv preprint arXiv:2103.15743* (2021).
 [9] J. Wrachtrup and F. Jelezko, *Journal of Physics: Condensed Matter* **18**, S807 (2006).
 [10] J. J. Longdell, E. Fraval, M. J. Sellars, and N. B. Manson, *Physical review letters* **95**, 063601 (2005).
 [11] M. Zhong, M. P. Hedges, R. L. Ahlefeldt, J. G. Bartholomew, S. E. Beavan, S. M. Wittig, J. J. Longdell, and M. J. Sellars,

- Nature **517**, 177 (2015).
- [12] A. Dibos, M. Raha, C. Phenicie, and J. D. Thompson, Physical review letters **120**, 243601 (2018).
- [13] T. Zhong, J. M. Kindem, E. Miyazono, and A. Faraon, Nature communications **6**, 8206 (2015).
- [14] S. Ourari, L. Dusanowski, S. P. Horvath, M. T. Uysal, C. M. Phenicie, P. Stevenson, M. Raha, S. Chen, R. J. Cava, N. P. de Leon, et al., Nature **620**, 977 (2023).
- [15] L. Nicolas, M. Businger, T. Sanchez Mejia, A. Tiranov, T. Chanelière, E. Lafitte-Houssat, A. Ferrier, P. Goldner, and M. Afzelius, npj Quantum Information **9**, 21 (2023).
- [16] A. Tiranov, A. Ortu, S. Welinski, A. Ferrier, P. Goldner, N. Gisin, and M. Afzelius, Physical Review B **98**, 195110 (2018).
- [17] J. M. Kindem, J. G. Bartholomew, P. J. Woodburn, T. Zhong, I. Craiciu, R. L. Cone, C. W. Thiel, and A. Faraon, Physical Review B **98**, 024404 (2018).
- [18] S. Welinski, A. Ferrier, M. Afzelius, and P. Goldner, Physical Review B **94**, 155116 (2016).
- [19] A. Ortu, A. Tiranov, S. Welinski, F. Fröwis, N. Gisin, A. Ferrier, P. Goldner, and M. Afzelius, Nature materials **17**, 671 (2018).
- [20] S. Welinski, A. Tiranov, M. Businger, A. Ferrier, M. Afzelius, and P. Goldner, Physical Review X **10**, 031060 (2020).
- [21] M. Businger, A. Tiranov, K. T. Kaczmarek, S. Welinski, Z. Zhang, A. Ferrier, P. Goldner, and M. Afzelius, Physical review letters **124**, 053606 (2020).
- [22] M. Businger, L. Nicolas, T. S. Mejia, A. Ferrier, P. Goldner, and M. Afzelius, Nature communications **13**, 6438 (2022).
- [23] F. Chioffi, E. Lafitte-Houssat, A. Ferrier, S. Welinski, L. Morvan, P. Berger, D. Serrano, M. Afzelius, and P. Goldner, Physical Review B **109**, 094114 (2024).
- [24] U. Ranon, Physics Letters A **28**, 228 (1968).
- [25] C. Kränkel, D. Fagundes-Peters, S. Fredrich, J. Johannsen, M. Mond, G. Huber, M. Bernhagen, and R. Uecker, Applied Physics B **79**, 543 (2004).
- [26] J. G. Bartholomew, J. Rochman, T. Xie, J. M. Kindem, A. Ruskuc, I. Craiciu, M. Lei, and A. Faraon, Nature communications **11**, 3266 (2020).
- [27] A. Ruskuc, C.-J. Wu, J. Rochman, J. Choi, and A. Faraon, Nature **602**, 408 (2022).
- [28] T. Xie, R. Fukumori, J. Li, and A. Faraon, arXiv preprint arXiv:2407.08879 (2024).
- [29] R. W. Equall, Y. Sun, R. Cone, and R. Macfarlane, Physical review letters **72**, 2179 (1994).
- [30] T. Zhong, J. Rochman, J. M. Kindem, E. Miyazono, and A. Faraon, Optics express **24**, 536 (2016).
- [31] J. M. Kindem, A. Ruskuc, J. G. Bartholomew, J. Rochman, Y. Q. Huan, and A. Faraon, Nature **580**, 201 (2020).
- [32] C.-J. Wu, D. Riedel, A. Ruskuc, D. Zhong, H. Kwon, and A. Faraon, Physical Review Applied **20**, 044018 (2023).
- [33] E. Fraval, M. J. Sellars, and J. Longdell, Physical review letters **95**, 030506 (2005).
- [34] L. Rippe, B. Julsgaard, A. Walther, Y. Ying, and S. Kröll, Physical Review A—Atomic, Molecular, and Optical Physics **77**, 022307 (2008).
- [35] J. Longdell, M. Sellars, and N. Manson, Physical review letters **93**, 130503 (2004).
- [36] J. H. Wesenberg, K. Mølmer, L. Rippe, and S. Kröll, Physical Review A **75**, 012304 (2007).
- [37] A. Walther, B. Julsgaard, L. Rippe, Y. Ying, S. Kröll, R. Fisher, and S. Glaser, Physica Scripta **2009**, 014009 (2009).
- [38] A. Walther, L. Rippe, Y. Yan, J. Karlsson, D. Serrano, A. Nilsson, S. Bengtsson, and S. Kröll, Physical Review A **92**, 022319 (2015).
- [39] A. Kinos, L. Rippe, S. Kröll, and A. Walther, Physical Review A **104**, 052624 (2021).
- [40] A. Kinos, L. Rippe, D. Serrano, A. Walther, and S. Kröll, Physical Review A **105**, 032603 (2022).
- [41] R. Kolesov, K. Xia, R. Reuter, R. Stöhr, A. Zappe, J. Meijer, P. Hemmer, and J. Wrachtrup, Nature communications **3**, 1029 (2012).
- [42] C. Yin, M. Rancic, G. G. de Boo, N. Stavrias, J. C. McCallum, M. J. Sellars, and S. Rogge, Nature **497**, 91 (2013).
- [43] L. Yang, S. Wang, M. Shen, J. Xie, and H. X. Tang, Nature Communications **14**, 1718 (2023).
- [44] T. Zhong, J. M. Kindem, J. G. Bartholomew, J. Rochman, I. Craiciu, V. Verma, S. W. Nam, F. Marsili, M. D. Shaw, A. D. Beyer, et al., Physical review letters **121**, 183603 (2018).
- [45] A. Ruskuc, C.-J. Wu, E. Green, S. L. Hermans, J. Choi, and A. Faraon, arXiv preprint arXiv:2402.16224 (2024).
- [46] N. Ohlsson, R. K. Mohan, and S. Kröll, Optics communications **201**, 71 (2002).
- [47] F. K. Asadi, N. Lauk, S. Wein, N. Sinclair, C. O'Brien, and C. Simon, Quantum **2**, 93 (2018).
- [48] M. Grimm, A. Beckert, G. Aepli, and M. Müller, Prx Quantum **2**, 010312 (2021).
- [49] F. K. Asadi, S. Wein, and C. Simon, Physical Review A **102**, 013703 (2020).
- [50] A. M. Childs, Lecture notes at University of Maryland **5** (2017).
- [51] G. Lindblad, Communications in mathematical physics **48**, 119 (1976).
- [52] S. C. Wein, J.-W. Ji, Y.-F. Wu, F. Kimiaee Asadi, R. Ghobadi, and C. Simon, Physical Review A **102**, 033701 (2020).
- [53] F. K. Asadi, S. Wein, and C. Simon, Quantum Science and Technology **5**, 045015 (2020).
- [54] R. Blume-Kohout, M. P. da Silva, E. Nielsen, T. Proctor, K. Rudinger, M. Sarovar, and K. Young, PRX Quantum **3**, 020335 (2022).
- [55] Y. Q. Huan, J. M. Kindem, J. G. Bartholomew, and A. Faraon, in CLEO: QELS Fundamental Science (Optica Publishing Group, 2019) pp. JTu2A-26.
- [56] A. Abragam and B. Bleaney, Electron paramagnetic resonance of transition ions (Oxford University Press, 2012).
- [57] L.-M. Duan, B. Wang, and H. Kimble, Physical Review A **72**, 032333 (2005).
- [58] S. D. Barrett and P. Kok, Physical Review A **71**, 060310 (2005).
- [59] X.-M. Lin, Z.-W. Zhou, M.-Y. Ye, Y.-F. Xiao, and G.-C. Guo, Physical Review A **73**, 012323 (2006).
- [60] S. Welte, B. Hacker, S. Daiss, S. Ritter, and G. Rempe, Physical Review X **8**, 011018 (2018).
- [61] Y.-F. Xiao, X.-M. Lin, J. Gao, Y. Yang, Z.-F. Han, and G.-C. Guo, Physical Review A **70**, 042314 (2004).
- [62] C. O'Brien, T. Zhong, A. Faraon, and C. Simon, Physical Review A **94**, 043807 (2016).
- [63] A. Reiserer, N. Kalb, M. S. Blok, K. J. van Bemmelen, T. H. Taminiou, R. Hanson, D. J. Twitchen, and M. Markham, Physical Review X **6**, 021040 (2016).
- [64] J.-W. Ji, Y.-F. Wu, S. C. Wein, F. K. Asadi, R. Ghobadi, and C. Simon, Quantum **6**, 669 (2022).
- [65] Y. L. Lim, A. Beige, and L. C. Kwak, Physical review letters **95**, 030505 (2005).
- [66] S. C. Wein, arXiv preprint arXiv:2105.06580 (2021).
- [67] T. Kornher, K. Xia, R. Kolesov, N. Kukharchyk, R. Reuter, P. Silyushev, R. Stöhr, M. Schreck, H.-W. Becker, B. Villa, et al., Applied Physics Letters **108** (2016).
- [68] S. Goswami, K. Heshami, and C. Simon, Physical Review A **98**, 043842 (2018).

- [69] H. Bernien, B. Hensen, W. Pfaff, G. Koolstra, M. S. Blok, L. Robledo, T. H. Taminiau, M. Markham, D. J. Twitchen, L. Childress, *et al.*, *Nature* **497**, 86 (2013).
- [70] J. Majer, J. Chow, J. Gambetta, J. Koch, B. Johnson, J. Schreier, L. Frunzio, D. Schuster, A. A. Houck, A. Wallraff, *et al.*, *Nature* **449**, 443 (2007).
- [71] A. Blais, R.-S. Huang, A. Wallraff, S. M. Girvin, and R. J. Schoelkopf, *Physical Review A* **69**, 062320 (2004).
- [72] L. S. Martin and K. B. Whaley, *arXiv preprint arXiv:1912.00067* (2019).
- [73] Note that we are implicitly using the fact that $\rho_I(0) = \rho(0) = |\psi(0)\rangle\langle\psi(0)|$.
- [74] M. Horodecki, P. Horodecki, and R. Horodecki, *Physical Review A* **60**, 1888 (1999).
- [75] M. A. Nielsen, *Physics Letters A* **303**, 249 (2002).
- [76] J. Combes, J. Kerckhoff, and M. Sarovar, *Advances in Physics: X* **2**, 784 (2017).

SUPPLEMENTARY MATERIAL

SI. PERTURBATIVE FIDELITY COMPUTATION

In this section, we elaborate on our techniques presented in [Section IV](#). We show how one can compute the infidelity up to the desired order, and in particular, we provide a derivation for [Equation \(8\)](#), [Equation \(9\)](#), and [Equation \(10\)](#).

We rewrite [Equation \(5\)](#) as

$$\dot{\rho} = -\frac{i}{\hbar}[H_g + \delta\tilde{H}_e, \rho] + \mathcal{D}[\rho], \quad (\text{S1})$$

with $\mathcal{D}[\rho] = \sum_k \gamma_k L_k \rho L_k^\dagger - \frac{\gamma_k}{2} \{L_k^\dagger L_k, \rho\}$. More specifically, we may write \mathcal{D}_k as the superoperator considering the effects of the k -th term, i.e., $\mathcal{D}_k[\bullet] := L_k \bullet L_k^\dagger - \frac{1}{2} \{L_k^\dagger L_k, \bullet\}$. We then begin with considering evolution in the interaction picture. Let

$$\begin{aligned} \rho_I(t) &= U^\dagger(t) \rho(t) U(t) \\ \mathcal{D}_I[\bullet] &= U^\dagger(t) \mathcal{D}[U(t) \bullet U^\dagger(t)] U(t) \\ H_{e,I} &= U^\dagger(t) \tilde{H}_e U(t), \end{aligned} \quad (\text{S2})$$

where the unitary operator $U(t)$ is defined as $U(t) = \mathcal{T} \exp\left(-\frac{i}{\hbar} \int_0^{T_g} H(t') dt'\right)$, and the subscript I denotes quantities in the interaction picture. Moreover, we note the operator $\mathcal{D}_{k,I}$ can be written via $L_{k,I} = U(t) L_k U^\dagger(t)$ as

$$\mathcal{D}_I[\bullet] = \sum_k L_{k,I} \bullet L_{k,I}^\dagger - \frac{1}{2} \{L_{k,I}^\dagger L_{k,I}, \bullet\}. \quad (\text{S3})$$

Differentiating ρ_I with respect to time gives

$$\begin{aligned} \frac{d}{dt} \rho_I(t) &= U^\dagger(t) \frac{i}{\hbar} [H_g, \rho(t)] U(t) + U(t)^\dagger \dot{\rho}(t) U(t) \\ &\stackrel{(i)}{=} U(t)^\dagger \left(-\frac{i}{\hbar} \delta [H_e, \rho(t)] + \mathcal{D}[\rho(t)] \right) U(t) \\ &\stackrel{(ii)}{=} -\frac{i}{\hbar} \delta [H_{e,I}(t), \rho_I(t)] + \mathcal{D}_I[\rho_I(t)], \end{aligned} \quad (\text{S4})$$

where (i) follows from [Equation \(S1\)](#) and (ii) is due to [Equation \(S2\)](#). Furthermore, a simple calculation demonstrates that, employing the definition we provided in [Equation \(6\)](#), we obtain

$$F = \langle \psi(0) | \rho_I(T_g) | \psi(0) \rangle. \quad (\text{S5})$$

In order to compute $\rho_I(T_g)$, we note that one can obtain ρ_I at any time, say t , by rewriting [Equation \(S4\)](#) in the integral form [\[73\]](#)

$$\begin{aligned} \rho_I(t) &= \rho(0) - \frac{i\delta}{\hbar} \int_0^t [H_{e,I}(t'), \rho_I(t')] dt' \\ &\quad + \int_0^t \mathcal{D}_I(t') [\rho_I(t')] dt'. \end{aligned} \quad (\text{S6})$$

Using this equation recursively, we get the following first and second-order approximate solution

$$\begin{aligned} \rho_I^{(1)}(T_g) &= \rho(0) - \frac{i\delta}{\hbar} \int_0^{T_g} [H_{e,I}(t'), \rho(0)] dt' \\ &\quad + \int_0^{T_g} \mathcal{D}_I(t') [\rho(0)] dt' \quad (\text{1st order}), \end{aligned} \quad (\text{S7})$$

and

$$\begin{aligned} \rho_I^{(2)}(T_g) &= \rho(0) - \frac{i\delta}{\hbar} \int_0^{T_g} [H_{e,I}(t'), \rho^{(1)}(t)] dt' \\ &\quad + \int_0^{T_g} \mathcal{D}_I(t') [\rho^{(1)}(t)] dt' \quad (\text{2nd order}). \end{aligned} \quad (\text{S8})$$

More generally, one can recursively employ $\rho_I^{(j)}(T_g) = \frac{i\delta}{\hbar} \int_0^{T_g} [H_{e,I}(t'), \rho^{(j-1)}(t)] dt' + \int_0^{T_g} \mathcal{D}_I(t') [\rho^{(j-1)}(t)] dt'$ to obtain the j -th order approximation to $\rho_I(t)$. We note that the difference between $\rho_I(t)$ and $\rho_I^{(j)}(t)$ is of the order of $(|\delta| + \sum_k |\gamma_k|)^{j+1}$ i.e., $\|\rho_I(t) - \rho_I^{(j)}(t)\| = O(|\delta| + \sum_k |\gamma_k|)^{j+1}$. Using such expansions, together with [Equation \(S5\)](#) we get

$$F = 1 - \langle \psi(0) | \rho_I^{(j)} | \psi(0) \rangle + O\left(T_g^{j+1} \left(\frac{\|\tilde{H}_e\|}{\hbar} |\delta| + \sum_k |\gamma_k|\right)^{j+1}\right). \quad (\text{S9})$$

In what follows, we elaborate on the computation of [Equation \(S9\)](#) and demonstrate calculations that yield to [Equation \(8\)](#). Next, in [Section SI B](#), we consider the non-Hermitian perturbation to the Hamiltonian and derive [Equation \(9\)](#).

A. Derivation of [Equation \(8\)](#) and [Equation \(10\)](#)

Let us start by examining the fidelity for the first-order approximation $\rho_I^{(1)}$ in [Equation \(S7\)](#). This gives

$$\begin{aligned} 1 - F &= -\frac{i\delta}{\hbar} \int_0^{T_g} \langle \psi(0) | [H_{e,I}(t'), |\psi(0)\rangle \langle \psi(0)|] | \psi(0) \rangle \\ &\quad + \int_0^{T_g} \langle \psi(0) | \mathcal{D}_I[|\psi(0)\rangle \langle \psi(0)|] | \psi(0) \rangle \\ &\quad + O\left(T_g^2 \left(\frac{\|\tilde{H}_e\|}{\hbar} |\delta| + \sum_k |\gamma_k|\right)^2\right). \end{aligned} \quad (\text{S10})$$

Note that $\langle \psi(0) | [H_{e,I}(t'), |\psi(0)\rangle \langle \psi(0)|] | \psi(0) \rangle = 0$, which means that the first-order contribution of δ (i.e., reversible errors) to infidelity is zero. However, accounting for first-order irreversible errors, we have

$$\begin{aligned} \langle \psi(0) | \mathcal{D}_I[|\psi(0)\rangle \langle \psi(0)|] | \psi(0) \rangle &= \\ &= \sum_k \gamma_k \langle \psi(0) | L_{k,I} | \psi(0) \rangle \langle \psi(0) | L_{k,I}^\dagger | \psi(0) \rangle \\ &\quad - \frac{1}{2} \langle \psi(0) | \{L_{k,I}^\dagger L_{k,I}, |\psi(0)\rangle \langle \psi(0)|\} | \psi(0) \rangle, \end{aligned} \quad (\text{S11})$$

which follows directly from Equation (S3). Note that

$$\begin{aligned} \langle \psi(0) | L_{k,I} | \psi(0) \rangle &= \langle \psi(0) | U^\dagger(t) L_k U(t) | \psi(0) \rangle \\ &= \langle L_k(t) \rangle, \end{aligned} \quad (\text{S12})$$

as we are adapting the notation $\langle \mathcal{O}(t) \rangle := \langle \psi(t) | \mathcal{O} | \psi(t) \rangle$. Using a similar argument for the second term on the right-hand side of Equation (S11) we get

$$1 - F = \varepsilon_L^{(1)} + O\left(T_g^2 \left(\frac{\|\tilde{H}_e\|}{\hbar} |\delta| + \sum_k |\gamma_k| \right)^2\right), \quad (\text{S13})$$

with

$$\varepsilon_L^{(1)} = \sum_k \int_0^{T_g} \gamma_k \left(\langle L_k^\dagger(t') L_k(t') \rangle - |\langle L_k(t') \rangle|^2 \right) dt',$$

which is identical to Equation (8). We proceed to the second term correction by computing $\langle \psi(0) | \rho_I^{(2)} - \rho_I^{(1)} | \psi(0) \rangle$. Note that $\varepsilon_L^{(1)} + \langle \psi(0) | \rho_I^{(2)} - \rho_I^{(1)} | \psi(0) \rangle$ gives us the second order approximation to F . However, as we are merely interested in the first non-zero perturbation terms, we will keep only the terms including δ^2 and $\delta \cdot \gamma_k$ as the first-order contribution of δ is zero. We have

$$\begin{aligned} \rho_I^{(2)} - \rho_I^{(1)} &= -\frac{\delta^2}{\hbar^2} \int_0^{T_g} \int_0^t [H_{e,I}(t'), [H_{e,I}(t''), \rho_0]] dt' dt'' \\ &\quad - \frac{i\varepsilon}{\hbar} \left(\int_0^{T_g} \int_0^t [H_{e,I}(t'), \mathcal{D}_I(t'') [\rho(0)]] dt' dt'' \right. \\ &\quad \left. - \int_0^{T_g} \int_0^t \mathcal{D}_I(t') [[H_{e,I}(t'), \rho_0]] dt' dt'' \right) \\ &\quad + O(T_g^2 (\sum_k |\gamma_k|)^2) \\ &\quad + O\left(T_g^3 \left(\frac{\|\tilde{H}_e\|}{\hbar} |\delta| + \sum_k |\gamma_k| \right)^3\right). \end{aligned} \quad (\text{S14})$$

By a straightforward calculation, we get

$$\begin{aligned} \langle \psi_0 | [H_{e,I}(t'), [H_{e,I}(t''), \rho_0]] | \psi_0 \rangle &= \\ &= \text{Re} \left(\langle H_e(t') H_e(t'') \rangle \right. \\ &\quad \left. - \langle H_e(t') \rangle \langle H_e(t'') \rangle \right), \end{aligned} \quad (\text{S15})$$

which corresponds to $\varepsilon_{HH}^{(2)}$ as in Equation (10). Similarly, we get

$$\begin{aligned} -i \langle \psi_0 | [H_{e,I}(t'), \mathcal{D}_I[\rho_0]] | \psi_0 \rangle &= \\ &= \text{Im} \left(\sum_k \gamma_k \langle H_e(t') L_k(t'') \rangle \langle L_k(t'') \rangle \right. \\ &\quad \left. - 2 \langle H_e(t') L_k(t'') \rangle \langle L_k^\dagger(t'') \rangle \right), \end{aligned} \quad (\text{S16})$$

and

$$\begin{aligned} -i \langle \psi_0 | \mathcal{D}_I(t') [[H_{e,I}(t'), \rho_0]] | \psi_0 \rangle &= \\ &= \text{Im} \left(\langle L_k^\dagger(t') L_k(t') H_e(t'') \rangle \right. \\ &\quad \left. - 2 \langle L_k(t') H_e(t'') \rangle \langle L_k^\dagger(t'') \rangle \right), \end{aligned} \quad (\text{S17})$$

which gives

$$\begin{aligned} \varepsilon_{LH}^{(2)} &= \sum_k \frac{\gamma_k \delta}{\hbar} \int_{t'=0}^{T_g} \int_{t''=0}^{t'} \text{Im} \left(\langle H_e(t') L_k^\dagger(t'') L_k(t'') \rangle \right. \\ &\quad \left. - 2 \langle H_e(t') L_k(t'') \rangle \langle L_k^\dagger(t'') \rangle \right) dt'' dt' \\ &\quad + \sum_k \frac{\gamma_k \delta}{\hbar} \int_{t'=0}^{T_g} \int_{t''=0}^{t'} \text{Im} \left(\langle L_k^\dagger(t') L_k(t') H_e(t'') \rangle \right. \\ &\quad \left. - 2 \langle L_k(t') H_e(t'') \rangle \langle L_k^\dagger(t'') \rangle \right) dt'' dt'. \end{aligned} \quad (\text{S18})$$

B. Derivation of Equation (9)

We note that for a non-Hermitian perturbation, the evolution can be written as

$$\dot{\rho} = -\frac{i}{\hbar} ([H_g, \rho] + \delta(\tilde{H}_e \rho - \rho \tilde{H}_e^\dagger)) + \mathcal{D}[\rho], \quad (\text{S19})$$

where \tilde{H}_e is the non-Hermitian perturbation. Employing the approach introduced earlier to get Equation (S7), we find that

$$\begin{aligned} \rho_I^{(1)}(T_g) &= \rho(0) - \frac{i\delta}{\hbar} \int_0^{T_g} (H_{e,I}(t') \rho_0 - \rho_0 H_{e,I}^\dagger(t')) \\ &\quad + \int_0^{T_g} \mathcal{D}_I(t') [\rho(0)] dt'. \end{aligned} \quad (\text{S20})$$

A straightforward calculation yields

$$\begin{aligned} \langle \psi(0) | (H_{e,I}(t') \rho_0 - \rho_0 H_{e,I}^\dagger(t')) | \psi(0) \rangle &= \\ &= \langle \tilde{H}_e(t') \rangle - \langle \tilde{H}_e^\dagger(t') \rangle. \end{aligned}$$

This gives us the $\varepsilon_H^{(1)}$ as in Equation (9).

SII. AVERAGE GATE FIDELITY

In this section, we demonstrate how the state fidelity computation obtained through the perturbative approach can be extended to compute the average gate fidelity. To this end, we use the entanglement fidelity, which is closely connected to the average gate fidelity.

Let $\mathcal{E}[\bullet] = \mathcal{T} \exp\left(\int_0^{T_g} \mathcal{L}_I(t') dt'\right)[\bullet]$ be the channel representing the evolution under the interaction picture's Lindbladian. So far, we have considered the computation of

$$F_{\psi_0} = \langle \psi(0) | \mathcal{E}[\psi(0)] | \psi(0) \rangle \quad (\text{S21})$$

which is the fidelity of between the output state of the Lindbladian evolution and the ideal state of the computation, starting from $|\psi\rangle(0)$. However, in quantum computation, one is often interested in ‘gate fidelity.’ Important instances of gate fidelities include the minimum, average, and entanglement fidelity [4]. These three notions, in our case, can be formulated as

$$\begin{cases} F_{\min} = \min_{\psi} \langle \psi | \mathcal{E}[\psi] | \psi \rangle \\ F_{\text{avg}} = \int d\mu(\psi) \langle \psi | \mathcal{E}[\psi] | \psi \rangle \\ F_{\text{ent}} = \langle \phi | (\mathbb{I} \otimes \mathcal{E})[\phi] | \phi \rangle, \end{cases} \quad (\text{S22})$$

where F_{\min} , F_{avg} , and F_{ent} represent the minimum, average, and entanglement fidelity, respectively. Here, we use $|\phi\rangle$ to denote the maximally entangled state between the system and the ancilla (See Figure S1). Note that the entanglement fidelity (F_{ent}) is essentially the fidelity between the Choi matrix of \mathcal{E} and the maximally mixed state. Moreover, the measure μ in the definition of the average fidelity (F_{avg}) is the Haar measure. In what follows, we explain how our method can be extended to compute the entanglement and the average fidelities.

Regarding the entanglement fidelity, first note that $\mathbb{I} \otimes \mathcal{E}$ is the channel that can be realized by appending an identity to the Hamiltonian and the jump operators of our Lindbladian, and then the main method of Section SI can be applied with the initial state being the Choi matrix. More concretely, we get the following relations for the first-order errors

$$\begin{aligned} \varepsilon_{\text{ent},L}^{(1)} &= \sum_k \int_0^{T_g} \gamma_k \left(\langle \mathbb{I} \otimes L_k^\dagger(t') L_k(t') \rangle - |\langle \mathbb{I} \otimes L_k(t') \rangle|^2 \right) dt', \\ \varepsilon_{\text{ent},HH}^{(2)} &= \frac{2\delta^2}{\hbar^2} \int_0^{T_g} \int_0^{t'} \text{Re} \left(\langle \mathbb{I} \otimes H_e(t) H_e(t') \rangle \right. \\ &\quad \left. - \langle \mathbb{I} \otimes H_e(t) \rangle \langle \mathbb{I} \otimes H_e(t') \rangle \right) dt dt', \end{aligned} \quad (\text{S23})$$

Here, the expectations are taken with respect to the state $|\phi\rangle$, which is a tensor product of two ϕ^+ Bell states, and the \mathbb{I} operator in (S23), is a 4×4 operator as we consider two-dimensional registers as ancillae. Other formulas of the previous sections (such as $\varepsilon_{HL}^{(2)}$ and $\varepsilon_H^{(1)}$ for the case of non-Hermitian perturbation can be generalized similarly).

Finally, we point out that the average fidelity and the entanglement fidelity are related by the following elegant relation [74, 75]

$$F_{\text{avg}} = \frac{DF_{\text{ent}} + 1}{D + 1}, \quad (\text{S24})$$

where D is the effective system size (in our case $D = 4$ as we are effectively have two-qubits). Therefore, we have that the average gate infidelity $\varepsilon_{\text{avg}} = 1 - F_{\text{avg}}$ is related to the entanglement fidelity (ε_{ent}) via

$$\varepsilon_{\text{avg}} = \frac{D}{D+1} \varepsilon_{\text{ent}}. \quad (\text{S25})$$

As an example, we compute the average gate fidelity of the magnetic dipolar interaction gate scheme, as shown in

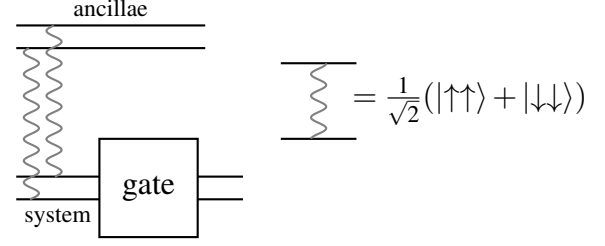


FIG. S1. The circuit computing the Choi matrix. Note that the ancillae are 2 dimensional registers and that the squiggling lines demonstrate the Bell state $|\phi^+\rangle = \frac{1}{\sqrt{2}}(|\uparrow\uparrow\rangle + |\downarrow\downarrow\rangle)$. The entanglement fidelity (F_{avg}) of a gate is the fidelity between the Choi matrices of the ideal channel and its implementation. A simple formulation is provided in (S22). Moreover, one can readily translate entanglement fidelity to average fidelity via (S24).

Section SIV. Additionally, we compare the state fidelity and average gate fidelity for this scheme, both obtained using the perturbative method.

SIII. STATE FIDELITY CALCULATION OF MAGNETIC DIPOLAR INTERACTION GATE SCHEME

To compute the fidelity of the magnetic dipolar gate, we employ the perturbative method outlined in Section IV, with the detailed derivation provided in Section SI. This involves solving the Schrödinger equation to derive the ideal gate evolution and evaluating the lowest-order error expressions. We also numerically solve the full system’s master equation for a realistic set of parameters to verify the analytic approximation. Figure S2 compares the two solutions and demonstrates that our approach effectively captures the infidelities as expected.

The magnetic dipole-dipole interaction phase gate can be broken down into three steps: activation, interaction, and deactivation. To obtain an analytic solution for the state evolution for the ideal gate, we assume that the activation (deactivation) step is performed using a square pulse with a temporal width T_{act} ($T_{\text{deact}} = T_{\text{act}}$) that is much shorter than the interaction time T_{int} . This allows us to separate the evolution over the gate time $T_{g,MD} = 2T_{\text{act}} + T_{\text{int}}$ into three piecewise time-independent operations that can each be solved analytically. That is, we assume that the ions are essentially decoupled during the activation and deactivation steps.

The total Hamiltonian of the system is given by

$$H(t) = H_0 + H_{\text{int}} + H_P(t), \quad (\text{S26})$$

where $H_0 = \sum_n (\omega_\uparrow |\uparrow\rangle \langle \uparrow| + \omega_{\uparrow'} |\uparrow'\rangle \langle \uparrow'| + \omega_{\downarrow'} |\downarrow'\rangle \langle \downarrow'|)_n$ is the free Hamiltonian with $n = \{\text{Yb}_1, \text{Yb}_2\}$. In the rotating frame defined by H_0 , the driving Hamiltonian becomes time-independent $H'_P = \sum_n \left(\frac{\Omega_{\uparrow}}{2} (\sigma_{\uparrow} + \sigma_{\uparrow'}) + \frac{\Omega_{\downarrow}}{2} (\sigma_{\downarrow} + \sigma_{\downarrow'}) \right)_n$,

where

$$\begin{aligned}\sigma_{\uparrow} &= |\uparrow'\rangle \langle \uparrow|, \sigma_{\uparrow'} = (\sigma_{\uparrow})^\dagger, \\ \sigma_{\downarrow} &= |\downarrow'\rangle \langle \downarrow|, \sigma_{\downarrow'} = (\sigma_{\downarrow})^\dagger.\end{aligned}$$

Here subscripts \uparrow, \downarrow indicate transitions $|\uparrow\rangle \mapsto |\uparrow'\rangle$ and $|\downarrow\rangle \mapsto |\downarrow'\rangle$, while the subscripts \uparrow', \downarrow' represent the reverse transitions $|\uparrow'\rangle \mapsto |\uparrow\rangle$ and $|\downarrow'\rangle \mapsto |\downarrow\rangle$ respectfully. Without loss of generality, we assume $(\Omega_{\uparrow, \downarrow})_n \geq 0$. In this rotating frame, the interaction Hamiltonian remains unchanged and is governed by the magnetic dipole-dipole interaction between two Yb ions (labelled with 1 and 2), as

$$H_{\text{int}} = \frac{\mu_0}{4\pi r^3} \left[\boldsymbol{\mu}_1 \cdot \boldsymbol{\mu}_2 - \frac{3(\boldsymbol{\mu}_1 \cdot \mathbf{r})(\boldsymbol{\mu}_2 \cdot \mathbf{r})}{r^2} \right], \quad (\text{S27})$$

where μ_0 is the vacuum permeability, $\boldsymbol{\mu}$ is the electronic magnetic dipole moment which is defined as $\boldsymbol{\mu} = \mu_B \cdot \mathbf{g} \cdot \mathbf{S}$, with μ_B being the Bohr magneton, and \mathbf{g} is g tensor with principal values of g_i (for $i = x, y, z$). Here \mathbf{r} is the distance between two ions in the crystal, where we assume two ions are located along the z-axis (c axis of the YVO crystal). In cases of imperfect alignment along the z-axis, additional error terms arise. However, these coherent errors stem from a Hamiltonian associated with a unitary evolution. As a result, these errors can, in principle, be mitigated by applying local operations to each qubit. We consider the point symmetry with $g_x \simeq g_y \equiv g_\perp$, and $g_z \equiv g_\parallel$. While g_\perp governs the transverse parts of the interaction (such as the spin flip-flop process), we compute the errors arising from these transverse interactions in detail. Therefore, we divide the interaction Hamiltonian into two parts

$$H_{\text{int}} = H_I + H_e, \quad (\text{S28})$$

with

$$H_I = J_\parallel Z_1 \otimes Z_2, \quad H_e = J_x X_1 \otimes X_2 + J_y Y_1 \otimes Y_2,$$

where H_I is an Ising-type interaction with coupling strength $J_\parallel = \frac{-\mu_0(\mu_B g_\parallel)^2}{8\pi r^3}$ and X, Y, Z represent Pauli matrices. The transverse interactions are given with H_e , where $J_i = \frac{\mu_0(\mu_B g_i)^2}{16\pi r^3}$ (for $i = x, y$) is the transverse interaction strength.

The reduced magnetic dipole-dipole interaction (denoted by H_I) can be exploited to execute the gate by use of the non-trivial unitary evolution of the active qubits ($U_I(t) = e^{-iH_I t}$). The activation and deactivation steps can be approximated by the evolution $U_P(t) = e^{-iH_P t}$ in the rotating frame. With these pieces, we can write the total gate propagator (i.e., the unitary) describing the evolution as follows

$$U_g(t) = \begin{cases} U_P(t) & 0 \leq t \leq T_{\text{act}} \\ U_I(t - T_{\text{act}}) U_P(T_{\text{act}}) & 0 < t - T_{\text{act}} \leq T_{\text{int}} \\ U_P(t - T_{\text{act}} - T_{\text{int}}) U_I(T_{\text{int}}) U_P(T_{\text{act}}) & t > T_{\text{act}} + T_{\text{int}} \end{cases} \quad (\text{S29})$$

Therefore, the final state after the evolution is

$$|\psi(T_g)\rangle = U_g(T_g) |\psi(0)\rangle. \quad (\text{S30})$$

For this gate analysis, the sources of error are the transverse dipole-dipole interaction described by the Hermitian Hamiltonian H_e and any decoherence processes such as spontaneous emission and dephasing. Thus, we can immediately conclude that $\varepsilon_H^{(1)} = 0$ and focus on the first-order term $\varepsilon_L^{(1)}$ and the second-order term $\varepsilon_{HH}^{(2)}$.

To evaluate the irreversible error $\varepsilon_L^{(1)}$, we consider equal optical spontaneous emission rates for each ion, denoted by $\gamma_{1, \uparrow'} (\gamma_{1, \downarrow'})$, that causes decay across the transition $|\uparrow'\rangle \mapsto |\uparrow\rangle$ ($|\downarrow'\rangle \mapsto |\downarrow\rangle$) with the corresponding Lindblad collapse operator $\sigma_{\uparrow'} (\sigma_{\downarrow'})$. We also consider a spin relaxation rate γ_2 (γ_3) that refers to the ground (excited) state spin-flip corresponding to the Lindblad operator $|\uparrow\rangle \langle \downarrow|$ ($|\uparrow'\rangle \langle \downarrow'\rangle$) and a spin pure dephasing rate γ_4 (γ_5) of the ground (excited) state spin doublet corresponding to Lindblad operator $|\downarrow\rangle \langle \downarrow| - |\uparrow\rangle \langle \uparrow|$ ($|\downarrow'\rangle \langle \downarrow'| - |\uparrow'\rangle \langle \uparrow'|$). Putting these together, we evaluate $\varepsilon_L^{(1)}$ given in Equation (8) using the ideal gate propagator in Equation (S29) to arrive at

$$\begin{aligned}\varepsilon_L^{(1)} &= T_{\text{act}} \left(\frac{7}{8} (\gamma_{1, \uparrow'} + \gamma_{1, \downarrow'}) + \frac{13}{16} (\gamma_2 + \gamma_3) + \frac{1}{2} (\gamma_4 + \gamma_5) \right) \\ &\quad + T_{\text{int}} \left(\gamma_{1, \uparrow'} + \gamma_{1, \downarrow'} + \frac{3}{4} \gamma_3 + \frac{1}{2} \gamma_5 \right),\end{aligned} \quad (\text{S31})$$

where we have assumed $\Omega_{\uparrow} = \Omega_{\downarrow} = \Omega = \pi/T_{\text{act}}$ and $T_{\text{int}} = \hbar\pi/4J_\parallel$.

For the reversible error, we evaluate Equation (10) using the error Hamiltonian given by H_e in Equation (S28) along with the ideal unitary propagator to obtain

$$\varepsilon_{HH}^{(2)} = \frac{a(J_x + J_y)^2}{J_z^2}, \quad (\text{S32})$$

where the coefficient is $a = (32(2 - \sqrt{2}) - \pi^2)/64$. For clarity, we add that the ideal Hamiltonian evolution considered in the computation of Equation (S32), is the $Z \otimes Z$ interaction term together with the free Hamiltonian. In the absence of free Hamiltonian, the expression would be much simpler as the error term $X \otimes X + Y \otimes Y$ commutes with $Z \otimes Z$. However, due to the presence of the free Hamiltonian, we end up with the more complex pre-factor a in Equation (S32). Substituting the Yb system's parameters, we find that the transverse interaction strength, $J_x = J_y \equiv J_\perp$, is 4.35 times weaker than the longitudinal interaction strength, $J_z \equiv J_\parallel$. Consequently, the contribution of second-order errors in Equation (S32) to the state fidelity equation is approximately 10^{-2} , supporting the validity of our assumption that it can be treated perturbatively.

Furthermore, Figure S2 presents a comparison between the fidelities obtained by simulating the exact system (i.e., solving the master equation) and those obtained from our perturbative solution. This comparison confirms that the two approaches yield consistent results within the expected ranges of r . Figure S2 provides additional insights into the ion separation regime of interest for the Yb:YVO system. Firstly, at small r , the dipolar interaction affects the excitation pulse

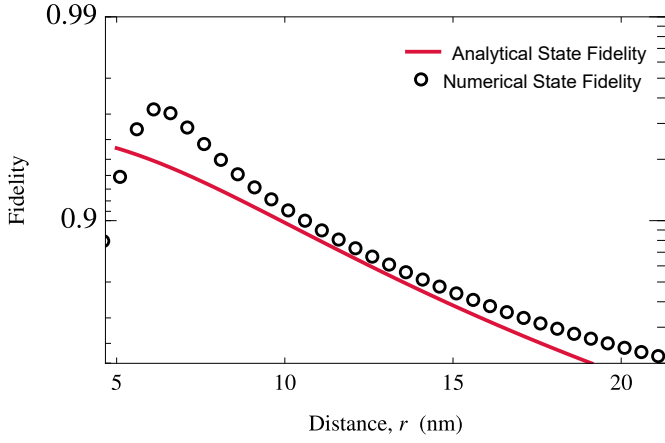


FIG. S2. State fidelity of the magnetic dipolar interaction gate as a function of the distance between ions. The analytic approximation using time-dependent perturbation theory including first and second-order errors (red curve) matches closely with the numerical simulation of the exact master equation dynamics (black circles). The numerical simulation, based on the parameters provided in Section V A of the main text, indicates that the maximum achievable fidelity, approximately 0.97, occurs at around $r \sim 6$ nm.

in a non-trivial way which is not captured by our analytical approach. This complex behavior, however, is evident in the numerical simulation. Note that the dipolar gate's non-trivial effect can be safely ignored when $\|H_{\text{int}}T_{\text{act}}\| \ll 1$, which corresponds to large enough r (e.g., $r \gtrsim 5$ nm with the existing parameters for Yb:YVO system). Secondly, for sufficiently large distances (e.g., greater than 20 nm for the system under study), the two solutions diverge. This occurs because the perturbative approach does not hold in the low-fidelity regime corresponding to longer interaction times (we recall that according to the perturbation solution in Equation (11) the fidelity scales as $\propto 1 - O(r^3)$ with interaction time $T_{\text{int}} \propto r^3$).

SIV. COMPARISON BETWEEN STATE FIDELITY AND AVERAGE GATE FIDELITY OF MAGNETIC DIPOLAR GATE SCHEME UTILIZING PERTURBATIVE METHOD

Here we compute the average gate fidelity of the magnetic dipolar interaction scheme (introduced in Section III A), utilizing the equations presented in Section III. The results of this calculation are brought in Figure S3, where we compare the state fidelity against the average gate fidelity. We observe that the two fidelities are comparable and have similar behaviour in the considered range of parameters.

SV. IMPLEMENTATION OF A CONTROLLED-Z GATE BASED ON PHOTON INTERFERENCE-BASED SCHEME

Following [65], one can apply a CZ gate using different measurement setups. Let the first and the second ion be ini-

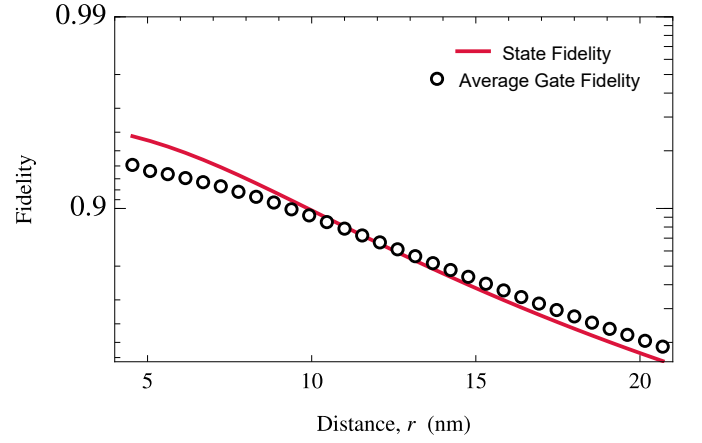


FIG. S3. Analytical state fidelity (red curve) and the average gate fidelity (black curve) of the magnetic dipolar interaction two-qubit phase gate as a function of ions' separation. We note that although the average gate fidelity is also obtained with the time-dependent perturbative method, we solve the integrals numerically, as the system size for this simulation is much larger (we have a 64-dimensional space), making symbolic computation extremely difficult. The parameters utilized are detailed in Section V A of the main text.

tially described by the arbitrary joint state

$$|\psi_{\text{init}}\rangle = \alpha |\uparrow_{Yb_1} \uparrow_{Yb_2}\rangle + \beta |\uparrow_{Yb_1} \downarrow_{Yb_2}\rangle + \gamma |\downarrow_{Yb_1} \uparrow_{Yb_2}\rangle + \delta |\downarrow_{Yb_1} \downarrow_{Yb_2}\rangle. \quad (\text{S33})$$

After excitation $|\uparrow\rangle \mapsto |\uparrow'\rangle$ and spontaneous emission steps, we get the following joint entangled state of the ions and photons

$$|\psi_{\text{ent}}\rangle = \alpha |\uparrow_{Yb_1} \uparrow_{Yb_2}\rangle |1_{Yb_1} 1_{Yb_2}\rangle + \beta |\uparrow_{Yb_1} \downarrow_{Yb_2}\rangle |1_{Yb_1} 0_{Yb_2}\rangle + \gamma |\downarrow_{Yb_1} \uparrow_{Yb_2}\rangle |0_{Yb_1} 1_{Yb_2}\rangle + \delta |\downarrow_{Yb_1} \downarrow_{Yb_2}\rangle |0_{Yb_1} 0_{Yb_2}\rangle. \quad (\text{S34})$$

Instead of measuring in the number basis of photons, we can measure in a mutually unbiased basis (MUB), where the measurement projects onto states of the following form of the cavities

$$|\Phi_{\text{meas}}\rangle = \frac{1}{2} \left(e^{i\phi_1} |0_{Yb_1} 0_{Yb_2}\rangle + e^{i\phi_2} |0_{Yb_1} 1_{Yb_2}\rangle + e^{i\phi_3} |1_{Yb_1} 0_{Yb_2}\rangle + e^{i\phi_4} |1_{Yb_1} 1_{Yb_2}\rangle \right). \quad (\text{S35})$$

Note that

$$(\mathbb{I} \otimes \langle \Phi_{\text{meas}} |) |\psi_{\text{ent}}\rangle \propto e^{-i\phi_1} \alpha |\uparrow_{Yb_1} \uparrow_{Yb_2}\rangle + e^{-i\phi_2} \beta |\uparrow_{Yb_1} \downarrow_{Yb_2}\rangle + e^{-i\phi_3} \gamma |\downarrow_{Yb_1} \uparrow_{Yb_2}\rangle + e^{-i\phi_4} \delta |\downarrow_{Yb_1} \downarrow_{Yb_2}\rangle. \quad (\text{S36})$$

Hence, post selecting on the state of the cavities being $|\Phi_{\text{meas}}\rangle$, we are effectively applying the gate $\text{diag}(e^{-i\phi_1}, e^{-i\phi_2}, e^{-i\phi_3}, e^{-i\phi_4})$. Choosing $\phi_1 = \phi_2 = \phi_3 = 0$ with $\phi_4 = \pi$ implements the controlled-Z gate.

SVI. FIDELITY CALCULATION OF PHOTON SCATTERING GATE SCHEME

Our method for computing the fidelity of the photon scattering scheme is based on the so-called SLH formalism [76], which stands for Scattering matrix, Lindblad operators, and Hamiltonian. This formalism allows to easily construct quantum master equations that include cascaded interactions mediated by waveguide modes. In order to obtain the master equation, we consider a cascaded system where a single photon source is modelled by an ideal two-level emitter whose emission is cascaded into the cavity that contains both ions. In the single-excitation regime, the cavity can additionally be described by a two-level system. For the ions, since we assume one of the two transitions is far off resonant with the cavity, we approximate each of them using a three-level system. Thus, the total Hilbert space of the simulated system has a size $2 \times 2 \times 3 \times 3 = 36$, corresponding to a Fock-Liouville space of $36^2 = 1296$.

The evolution of the incoming single-photon pulse can be described by an SLH triple (S_s, \mathbf{L}_s, H_s) , where $S_s = \mathbb{I}$ is the identity operator, and $H_s = 0$ is the cavity Hamiltonian (here s stands for ‘source’). The Lindblad operators \mathbf{L}_s include $\sqrt{\Gamma_s} a_s$ as the only non-zero component, where $\Gamma_s = 1/T_{1p}$ is the scattered photon bandwidth and a_s is the source photon annihilation operator. The cavity-ion system is modelled by the SLH triple (S_0, \mathbf{L}_0, H_0) where $S_0 = \mathbb{I}$ and $H_0 = \sum_n \omega_n \sigma_{\uparrow n}^\dagger \sigma_{\uparrow n} + (\omega_n + \omega_e) \sigma_{\downarrow n}^\dagger \sigma_{\downarrow n} + \omega_g \sigma_{\uparrow \downarrow n}^\dagger \sigma_{\uparrow \downarrow n}$, where ω_n is the frequency between $|\uparrow\rangle$ and $|\uparrow'\rangle$, ω_e is the separation frequency between $|\uparrow'\rangle$ and $|\downarrow'\rangle$ in the excited state, and ω_g is the separation frequency between $|\uparrow\rangle$ and $|\downarrow\rangle$ in the ground state. The Lindblad operators are $\sigma_{\uparrow} |\uparrow'\rangle = |\uparrow\rangle$, $\sigma_{\downarrow} |\downarrow'\rangle = |\downarrow\rangle$, and $\sigma_{\uparrow \downarrow} |\downarrow\rangle = |\uparrow\rangle$. The collapse operators \mathbf{L}_0 corresponding to the emission of light are $(\sqrt{\kappa} a_c, \sqrt{\gamma_{\uparrow}} \sigma_{\uparrow}, \sqrt{\gamma_{\downarrow}} \sigma_{\downarrow})$ and we additionally include optical and spin decoherence modeled by the collapse operators $\sqrt{\gamma^*} \sigma_{\uparrow}^\dagger \sigma_{\uparrow}$, $\sqrt{\gamma_2} \sigma_{\uparrow, n}$, and $\sqrt{\gamma_4} \sigma_{\uparrow, n}^\dagger \sigma_{\uparrow, n}$ for both ions.

Using the cascade rules from [76], we have that the final triple is $(\mathbb{I}, \mathbf{L}, H)$, where $\mathbf{L} = \mathbf{L}_0 + \mathbf{L}_s$, and $H = H_0 + H_s + V$ with V being the cascaded interaction term. This final triple then defines a time-independent master equation $\dot{\rho} = \mathcal{L}\rho$, which is then solved by $\rho(t) = e^{\mathcal{L}t} \rho(0)$ for an initial state $\rho(0) = \rho_s(0) \otimes \rho_c(0) \otimes \rho_1(0) \otimes \rho_2(0)$ where $\rho_s(0) = |1\rangle\langle 1|$, $\rho_c(0) = |0\rangle\langle 0|$, $\rho_i(0) = |\psi(0)\rangle\langle \psi(0)|$, and $|\psi(0)\rangle = (|\uparrow\rangle + |\downarrow\rangle)/\sqrt{2}$.

Since we obtain the time-dependent solution (the virtual source cavity is not driven), the resulting photon that cascades into the cavity containing the ions will have a Lorentzian spectral shape. This method could be used along with a time-dependent $\Gamma_s(t)$ to shape the photon, but at the cost of a significantly increased simulation time.

On the other hand, a Lorentzian-shaped photon complicates the analytic solution using the method described in [49]. This is because Lorentzian shapes diverge under integration, and thus require a truncation. In any case we expect that in Equation (12), at least for $\alpha \ll 1$, only the relationship between σ_p and T_g depends on the exact shape of the photon.

In principle, it should be possible to obtain an analytic approximation of the fidelity directly from the cascaded master equation, perhaps using a modification of the perturbative approach but for cascaded systems. However, we have thus far failed to do so because the ideal gate evolution is irreversible. This could be a topic for future exploration.

SVII. FIDELITY CALCULATION OF VIRTUAL PHOTON EXCHANGE GATE SCHEME

The fidelity of the virtual photon exchange scheme was previously established by some of us in Ref [49]. However, the method used could not account for all dissipative parameters, which resulted in an upper bound on gate fidelity. Later, the authors in Refs [53, 66] used numerical computation to add the effect of optical pure dephasing rate to the fidelity. Using the theoretical framework outlined in Section IV and assuming that the system operates in the bad cavity limit and considering the adiabatic regime, we reproduce these results and provide an analytical formulation for the fidelity of the virtual photon exchange scheme.

In the case of virtual photon exchange, it is useful to model noise using an effective non-Hermitian Hamiltonian. This is because the ideal gate evolution arises due to the adiabatic elimination of the mediating cavity mode. From this perspective, the cavity decay rate causes a non-Hermitian component to arise in the effective ion-ion interaction Hamiltonian.

We begin by writing the total Hamiltonian for the three-body system

$$H = H_0 + H_C + H_I, \quad (\text{S37})$$

where

$$\begin{aligned} H_0 &= \sum_n \omega_n \sigma_{\uparrow n}^\dagger \sigma_{\uparrow n} + (\omega_n + \omega_e) \sigma_{\downarrow n}^\dagger \sigma_{\downarrow n} + \omega_g \sigma_{\uparrow \downarrow n}^\dagger \sigma_{\uparrow \downarrow n}, \\ H_C &= \omega_C a^\dagger a, \\ H_I &= \sum_n \sum_k g_{nk} (\sigma_{nk}^\dagger a + h.c.). \end{aligned} \quad (\text{S38})$$

Here $g_{\uparrow, n}$ is the cavity coupling rate of transition $(|\uparrow\rangle \mapsto |\uparrow'\rangle)_n$, $g_{\downarrow, n}$ is the cavity coupling rate of the transition $(|\downarrow\rangle \mapsto |\downarrow'\rangle)_n$. We also assume $g_{nk} = g$ is the same for both transitions in both Yb ions.

Let $\Delta_n = \omega_n - \omega_c$ be the detuning between the cavity and the n^{th} ion’s optical transition $|\uparrow\rangle \mapsto |\uparrow'\rangle$. In the high-cooperativity regime, a large cavity detuning $\Delta = \Delta_{\text{Yb}_1} \simeq \Delta_{\text{Yb}_2} + \delta_{eg}$ allows for a dispersive interaction to mediate the two-qubit gate. In this regime, the unitary operator describing the evolution can be solved by adiabatically eliminating the cavity mode to obtain the ion-ion interaction Hamiltonian H_{AE} valid when $\delta_{eg} \gg \Delta \gg g$ [49]. In the limit that $\Delta \rightarrow \infty$ and $\delta_{eg} \rightarrow \infty$, a control phase gate is perfectly implemented after an interaction time of $T_g = \pi\Delta/g^2$.

The true time evolution operator in the absence of irreversible errors is given by $U(t) = e^{-i\hat{H}t}$ and the final state is $|\psi(t)\rangle = U(t)|\psi(0)\rangle$. However, to use the perturbative

method, it is necessary to analytically solve the system governed by the perfect Hamiltonian $H_g = \lim_{\Delta, \delta_{eg} \rightarrow \infty} H_{AE}$ with an error Hamiltonian $H_e = H - H_g$. Due to the large detunings, the eigenvalues of H_e can be much larger than those of H , which violates the conditions to apply perturbation theory. Thus, it is necessary also to eliminate the cavity mode for the error Hamiltonian and use $H_e = H_{AE} - H_g$. Unfortunately, eliminating the cavity mode in this way also eliminates the direct cavity-emitter coupling and hence all impact due to the cavity decay is lost, which greatly modifies the qualitative features of the gate error.

To maintain a dependence on the cavity decay rate while deriving a valid perturbation, we first consider the effective non-Hermitian Hamiltonian $H_{\text{eff}} = H - i\frac{\kappa}{2}a^\dagger a$ of the three-body system. This effective Hamiltonian captures the amplitude damping effect due to the cavity in the Hamiltonian evolution, but neglects the stochastic jump of the cavity mode to the ground state. Luckily, such a jump forces the system to leave the expected computational space and thus can be neglected without affecting the state fidelity [49].

We then proceed to eliminate the cavity mode for the non-Hermitian Hamiltonian H_{eff} to obtain the error-prone interaction Hamiltonian $H_{\text{eff,AE}}$. The damping effect caused by the cavity decay rate on the effective coupling rate now appears as a non-Hermitian error Hamiltonian $\tilde{H}_e = H_g - H_{\text{eff,AE}}$. With this, we can evaluate the expressions in Equation (8) to obtain the non-zero first-order error terms while accounting for any additional decoherence terms impacting the emitter systems. Notably, unlike the method used in Ref. [49], this approach allows for the analytic evaluation of first-order errors due to optical pure dephasing of the emitters.

Following this procedure, we find

$$\begin{aligned} \varepsilon_L^{(1)} &= \frac{\pi\kappa}{2\Delta} + T_g\gamma_5 + \frac{21}{32}T_g\gamma^* \\ \varepsilon_H^{(1)} &= \frac{2\pi\Delta}{C\kappa}, \end{aligned} \quad (\text{S39})$$

where γ^* is optical dephasing rate equal for both ions, Δ is cavity detuning, $C = 4g^2/\kappa\gamma_1$ is cavity cooperativity, κ is cavity decay rate, and γ_5 is spin dephasing rate of the excited state for both ions. We use this notation to maintain consistency with the cooperativity definition in the main text and the notation in Equation (S31). This result is exactly the same as the expression obtained in [49] (except a factor of two which comes from fidelity definition) once considering the optimal detuning condition $2\Delta = \kappa\sqrt{C}$, but now we include pure dephasing terms. Thus, the perturbative approach demonstrated in this work offers a real practical advantage, particularly in terms of faster symbolic computation times, especially in higher-dimensional Hilbert spaces. Note that the study in [53] also considered the impact of optical pure dephasing for this gate, but the technique relied on numerical simulations of the master equation to infer the scaling constant. Here, the perturbative approach allows one to capture the effects of all dissipative parameters up to any arbitrary order analytically.

To validate the analytic approximation, we compare it to an exact numerical simulation of the master equation dynamics

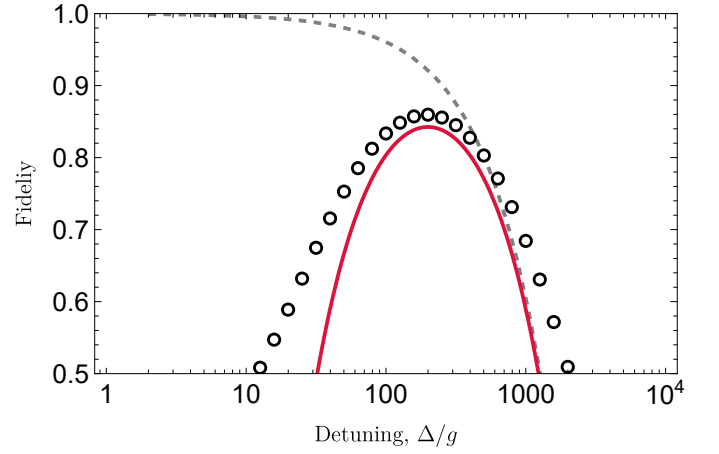


FIG. S4. State fidelity of the simple virtual photon exchange phase gate as a function of the cavity detuning Δ/g . The analytic approximation using first-order time-dependent perturbation theory (red curve) matches closely with the numerical simulation of the exact master equation dynamics (black circles) when fidelity is more than 0.8. The gray dashed line indicates the approximated error when neglecting the impact of cavity decay. The parameters used are $\kappa/g = 10$ indicating a weak cavity-emitter coupling regime, $\gamma_1 = 10^{-4}g$, $\delta_{eg} = 100g$, $\gamma^* = 10^{-4}g$, and $\gamma_5 = 10^{-5}g$ corresponding to a large cooperativity of $C = 4 \times 10^4$.

for parameters where all relevant sources of error are non-negligible (see Figure S4).